On the thermodynamics and its connection to structure in the Pt-Pd-Cu-Ni-P bulk metallic glass forming system

Nico Neuber[a*], Oliver Gross[b], Maximiliam Frey[a], Benedikt Bochtler[b], Alexander Kuball[b], Simon Hechler[b], Isabella Gallino[a] and Ralf Busch[a]

[a]*Chair of Metallic Materials, Saarland University, Campus C6.3, 66123 Saarbrücken, Germany*

[b]*Amorphous Metal Solution, Michellinstraße 9, 66424 Homburg, Germany*

*corresponding author

Abstract

Contrary to basic hard sphere structure models, recent studies revealed, significant structural differences between Pt-Cu-Ni-P and Pd-Cu-Ni-P metallic glass-forming liquids with the same stoichiometry. To cover the compositional space between both systems, Platinum is subsequently replaced by Palladium in the composition $(Pt/Pd)_{42.5}Cu_{27}Ni_{9.5}P_{21}$. For this systematic set of alloys, the thermodynamic properties, such as isobaric heat capacity, enthalpy and Gibbs free energy are assessed. A systematic drop of the Gibbs free energy difference between crystal and liquid, providing a lower estimate of the driving force for crystallization was observed, underlining the high glass-forming ability of the Pd-rich systems. Contrary to kinetic fragility data, a change of the thermodynamic fragility can be observed, drawing the picture of an increasing thermodynamically strong behavior with rising Pd-content. Further the temperature induced changes of the total structure factors S(Q) were monitored using high-energy synchrotron X-ray diffraction. Focus was laid on the changes on the medium-range length scale, by analyzing changes of the first sharp diffraction peak. Here a good correlation

25 of the changes in peak-width and the thermodynamic fragility was found. From the

26 determination of the excess enthalpy, large amounts of residual enthalpy in the glassy state

27 were observed for the Pt-rich alloys, supporting the increased ductility of these alloys. The

28 current findings further carve out the different roles of the topologically similar Pt and Pd in

29 the Pt/Pd-Cu-Ni-P alloy system and how the change of the structural motifs on the medium

30 range order is structurally influencing thermal properties such as enthalpy and heat capacity.

31

1. Introduction

The ability of a metallic melt to evade crystallization and eventually forming a glass when being cooled below its melting point has its origin in thermodynamic, kinetic and structural features of the system [1–4]. This implies a low driving force towards crystallization, sluggish kinetics and a high interfacial energy between the liquid and crystalline phase.

The structural evolution with decreasing temperature involves the formation and expansion of short- (SRO) and eventually medium-range order (MRO). However, the exact nature of these ordering processes is not fully understood. Simple hard sphere structural models of bulk glass-forming liquids are based on the efficient packing of representative structural units (clusters) [5]. In these models, elements with atomic radii that differ by no more than 2 % are considered as topologically equivalent [6]. According to this definition, Pd-Cu-Ni-P and Pt-Cu-Ni-P are topologically identical systems and the alloy compositions with the highest glass-forming ability (GFA) are found in the same compositional range [7], making them ideal "case-study" systems. However, the discrepancy in GFA (factor of four in critical thickness, 80 mm for $Pd_{42.5}Cu_{30}Ni_{7.5}P_{20}$ [8], 20 mm for $Pt_{42.5}Cu_{27}Ni_{9.5}P_{21}$ [9]) can neither be explained by the structural models nor by the very similar temperature dependence of the viscosity in the supercooled liquid (kinetic fragility)[10,11].

The decisive reasons, explaining the large difference in GFA, are found in the thermodynamic properties of the liquid, namely the interfacial energy between the liquid and the crystalline state as well as the driving force for crystallization [12], commonly approximated by the Gibbs free energy difference between the liquid and the crystal. The Pd-P-based liquids feature a small difference in Gibbs free energy between liquid and crystalline phase, resulting in an extremely low driving force for crystallization. In the Pt-P-based liquids a relatively large driving force for crystallization, normally leading to small GFA, is observed. For Pt-P based

57 liquids this is partially compensated by a high interfacial energy γ_{l-x} between the liquid and

58 crystalline phase, which increases the critical radius for nucleation r^* ($r^* \propto \gamma_{l-x}^3$) and hampers

59 the formation of critical nuclei, which leads to the high GFA in the Pt-based system [12].

60 The significant variation of the driving force for crystallization in both glass-forming liquids is

61 reflected in the pronounced increase in the entropy of fusion (factor of two) if Pd is replaced

62 by Pt. Although not entirely independent from the crystalline state, the striking change in the

63 entropy of fusion suggests that, contrary to the predictions of structural models, pronounced

64 structural differences between both liquid families must exist [11]. This is corroborated by

65 structural investigations, indicating that the local representative structural units and their

66 connection scheme varies, when Pd and Pt replace each other [13]. These structural differences,

67 leading to different connecting schemes between the clusters, could also be responsible for the

68 pronounced differences in sensitivity to cooling rate dependent and annealing induced

69 embrittlement of Pt-P-based and Pd-P-based liquids reported by Kumar et al. [14,15], i.e. they

70 might affect the topology of shear transformation zones and the formation of shear bands.

71 To systematically investigate the effect of the Pd/Pt concentration on thermo-physical

72 properties, twelve alloy compositions with different Pt/Pd ratios ($Pt_{42.5-x}Pd_xCu_{27}Ni_{9.5}P_{21}$, x =0

73 – 42.5 at %) are examined in an intensive calorimetry-based study. The glass transition,

74 crystallization and liquidus temperatures; the enthalpies of crystallization and melting, as well

75 as the specific isobaric heat capacity of glassy, crystalline and liquid state are determined and

76 used to calculate the thermodynamic functions of excess enthalpy, entropy and Gibbs free

77 energy between liquid and crystalline state as a function of Pt and Pd content. Furthermore,

78 non-isothermal high energy X-ray diffraction (HEXRD) structural data are used to connect the

79 thermodynamic behavior to structural changes in the deeply supercooled state. The

80 experiments yield a comprehensive data set of the thermodynamic and structural properties as

81 a function of the Pt/Pd concentration.

2. Experimental

2.1. Sample synthesis

For sample preparation, master alloys of $Pt_{42.5}Cu_{27}Ni_{9.5}P_{21}$ and $Pd_{42.5}Cu_{27}Ni_{9.5}P_{21}$ are produced by melting the high-purity raw elements (purity > 99.95%) under high-purity argon (Ar 6.0) atmosphere in a fused silica tube. Subsequently, the pre-alloys are heat-treated in dehydrated B_2O_3 for at least 16 hours at 1200 °C in a fused silica tube to remove impurities [16]. Afterwards, the master-alloys are mixed in the ratio of the desired compositions; $Pt_{42.5-x}Pd_xCu_{27}Ni_{9.5}P_{21}$ where x is x =0, 2.5, 7.5, 12.5, 17.5, 20, 22.5, 30, 40, 42.5 at%. In the following the specific alloys will be termed by their Pt and Pd content, e.g., *Pt22.5Pd20* for $Pt_{22.5}Pd_{20}Cu_{27}Ni_{9.5}P_{21}$. The solid mixture is then re-melted in an arc-melter under a high-purity argon atmosphere, to ensure a homogeneous sample. For both, the master-alloys and their derivatives, parts of the ingots are extracted for energy-dispersive X-ray analysis (EDX) measurements, to additionally monitor their composition and exclude experimental errors in compositional range.

The alloys are then inductively re-melted under a Ti-gettered high-purity argon atmosphere and subsequentially cast into water-cooled copper molds in a suction casting device to produce glassy plates with 0.5 mm thickness. The glassy character of the produced samples is initially confirmed by X-ray diffraction (XRD) with a PANalytical X'Pert Pro and later by synchrotron radiation based HEXRD at the P02.2 beamline with 60 keV at the Deutsche Elektronensynchrotron (DESY) (for a more detailed experimental description see section 2.3).

2.2. Thermal analysis

Thermal analysis is carried out using a power-compensated Perkin Elmer Hyper-DSC 8500 with a three-stage intra-cooler under constant flow of 20 ml/min high purity Ar (Ar 6.0). For

5

107 low temperature measurements up to a maximum temperature of 723 K, Al-pans are used,

108 whereas for examinations in higher temperature regions up to a maximum temperature of

109 973 K, including melting of the samples, graphite crucibles are utilized. For low temperature

110 measurements, each sample is remeasured after crystallization, enabling to use the signal of the

111 crystal as a baseline. Each melting curve is measured at least 5 times to account for

112 experimental uncertainty.

113 For measurements of the specific isobaric heat capacity, a step-method using a sapphire

114 standard as reference was applied, described in detail in Refs. [17,18]. In this method a heating

115 rate of 0.33 K s^{-1} with temperature steps of $\Delta T = 10$ K and equilibration times of $\Delta t = 120$ s are

116 chosen resulting in an effective heating rate of ~ 0.07 K s^{-1}.

117 According to this protocol, the heat capacity of the glass and supercooled liquid (SCL) is

118 determined in the first measurement run. Subsequently, the sample is heated to 750 K to ensure

119 a full crystallization of the amorphous fraction. This allows a second measurement run to

120 determine the heat capacity of the crystalline mixture. To increase the number of data points,

121 especially in the metastable region of the SCL, identical measurements on a new sample are

122 carried out with a temperature program shifted by 5 K. For assessments of the heat capacity in

123 the liquid state, the exact same samples are moved into graphite crucibles. Here the analogous

124 protocol is carried out in cooling, starting well above the liquidus temperatures of the respective

125 alloys at 973 K, until crystallization is interfering.

126 The specific isobaric heat capacities of the respective states are then modeled by

127
$$c_p^l(T) = 3R + aT + bT^{-2},\tag{1}$$

128 and

129
$$c_p^x(T) = 3R + cT + dT^2,\tag{2}$$

130 with R = 8.314 J mol^{-1} K^{-1} being the universal gas constant, a and b being fitting parameters of

131 the liquid (l), and c and d being fitting parameters for the crystal (x) [19].

2.3. High-energy synchrotron X-ray diffraction

High energy in-situ X-ray scattering experiments are carried out at the high resolution beamline P02.1 at PETRA III at the Deutsches Elektronen Synchrotron (DESY) in Hamburg [20]. For the measurements in transition geometry X-ray radiation with a wavelength of 0.207Å, corresponding to an energy of 60 keV, and a beam size of 0.8×0.8 mm^2 is used.

For the heating and cooling of the samples at a constant rate of 0.33 K s^{-1} a ceramic heater is utilized. The samples for measurements are cut from amorphous plate-shaped samples with a dimension of $1 \times 10 \times 13$ mm^3. They are placed in SiO_2 capillaries with a 1 mm diameter and a wall thickness of 0.01 mm. The sample is protected from oxidation by a constant flow of high purity Ar (Ar 5.0). Si-powder is used for a continuous temperature calibration of the furnace. A Perkin Elmer XRD1621 CsI bonded amorphous silicon detector (2048 pixels $\times$ 2048 pixels) records the diffraction pattern with an exposure time of 10 s, resulting in a temperature resolution of 3.3 K in the scans. The two-dimensional X-ray diffraction patterns are dark-subtracted and then integrated with the Fit2D data analysis software [21]. Background subtraction of the SiO_2 capillaries and further processing is done with the PDFgetX2 software [22]. For determination of the background pattern, room-temperature measurements are used, assuming it to be constant upon temperature changes. The data are corrected for sample absorption, polarization, and multiple scattering. The total structure factor S(Q) is calculated as [23]

$$S(Q) = 1 + \frac{I_C(Q) - \langle f(Q)^2 \rangle}{\langle f(Q) \rangle^2}, \tag{3}$$

where $I_C(Q)$ is the coherently scattered intensity, f(Q) is the atomic form factor, and Q is the scattering vector. The angle brackets signify a compositional average over all constituents. It shall be noted that the total structure factor contains all the structural information and is composed of n(n+1)/2 partial structure factors [24],

$$S(Q) = \sum_{i \leq j} w_{ij} S_{ij}(Q), \tag{4}$$

7

157 where w_{ij} is the weighting factor expressed as

158
$$w_{ij} = \frac{c_i c_j f_i(Q) f_j(Q)}{\langle f(Q) \rangle^2} \tag{5}$$

159 where c_i and c_j are the molar concentration of element i and j. However, it must be pointed out

160 that the main contribution to the scattering signal is provided by the elements with large

161 scattering lengths e.g., Pt and Pd.

162 The S(Q) data is evaluated using OriginLab2020b. For the peak analysis the peak was

163 interpolated using cubic splines, leading to an estimated uncertainty of 0.5 % based on

164 Ref. [25]. The samples are heated with 0.33 K s^{-1} to $T_{g,end}$ + 10 K well into the SCL region and

165 then cooled by the same rate to room-temperature. The heat-treatment is used to create a well-

166 defined enthalpic reference state and to exclude significant structural relaxation during the

167 actual measurement. Afterward this heat treatment the actual measurement is performed in a

168 second heating run with 0.33 K s^{-1} , covering the glass transition and full SCL region until the
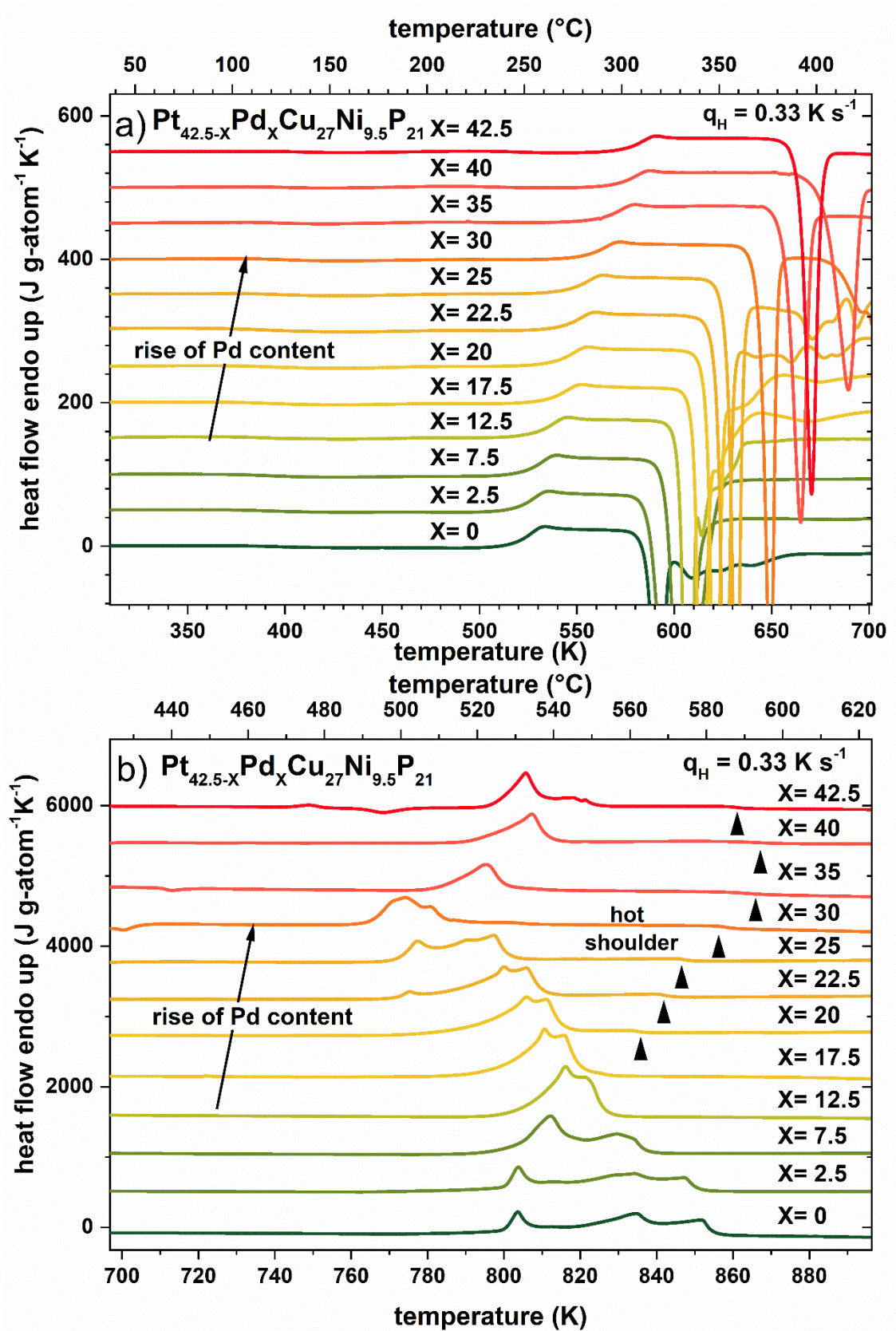
169 sample crystallized.

3. Results

3.1. Characteristic Temperatures and Enthalpies

Figure 1: a) DSC scan with 0.33 Ks^{-1} of Pt$_{42.5-x}$Pd$_x$Cu$_{27}$Ni$_{9.5}$P$_{21}$ with variations in Pd content (X) measured in Al pans up to 723 K giving a detailed view of the glass transition region as well as the crystallization event (exothermal peak). b) DSC scan with 0.33 Ks^{-1} of Pt$_{42.5-x}$Pd$_x$Cu$_{27}$Ni$_{9.5}$P$_{21}$ with variations in Pd content (X) measured in C crucibles up to 973 K depicting also the melting event (endothermal peak) of all alloys. The hot shoulder emerging at Pd contents x ≥ 17.5 at% is labeled and marked with black triangles. The triangles highlight the end of the shoulder-like heat flow signal during melting, which is corresponding to the liquidus temperature for each alloy.

A first step of examining the thermo-physical properties of amorphous metals is the monitoring of their respective characteristic temperatures, which are the glass transition temperature and the onset of crystallization, together with the enthalpy that is released during the crystallization. In Fig. 1a) the heat flow curves of all twelve different Pt/Pd-Cu-Ni-P based alloys during a DSC heating scan with 0.33 K s^{-1} obtained by differential scanning calorimetry are depicted. For each sample, the endothermal step of the glass transition is well visible. Here the initial glassy non-equilibrium state undergoes its transition to the metastable SCL state, detectable due to the increase in heat capacity generated by the change in configurations with temperature in the metastable liquid, as opposed to the glassy or crystalline state. The metastable plateau-like region of the SCL is then interrupted by a sudden exothermal event, the onset of crystallization. A clear shift of glass transition and onset of crystallization with increasing Pd content is observable. The growing length of the SCL region reflects an increasing resistance against crystallization with higher Pd content. In Fig. 2a) the evolution of the glass transition and onset of crystallization is depicted, showing a rather linear dependence with Pd content. Just the composition involving the least amount of Pt, *Pt2.5Pd40*, is posing an outlier by surpassing the *Pt0Pd42.5* alloy in thermal stability.

197 With changing Pd content the shape and area of the crystallization event changes in the

198 thermogram, i.e., the enthalpy of crystallization (Fig.2a)) decreases significantly through the

199 addition of Pd after a concentration of 22.5 at%. At this boundary concentration a drop of

200 almost 50% can be observed comparing *Pt20Pd22.5* and *Pt7.5Pd35*. The detailed evolution of

201 the enthalpy of crystallization as a function of composition is provided on the left axis of

202 Fig. 2a).

203 When turning the focus on Fig. 1b) to higher temperatures beyond the crystallization event, the

204 (endothermal) melting of the crystalline mixture can be observed. Here changes in the solidus

205 and liquidus temperature and in the shape of the melting-event can be observed, too.

206 While the pure *Pt42.5Pd0* alloy is showing a (well-known) off-eutectic behavior with three

207 distinct melting events [12], a merging of the events can be seen until a Pd content of 17.5 at%

208 is reached. From there a high temperature shoulder of the melting peak, marked by an arrow in

209 Fig. 1b) is evolving, leading to an increase of the liquidus temperature, while the melting peak

210 is splitting up again to multiple events. Especially the onset of melting is shifted to lower

211 temperatures as another peak is starting to establish at around 770 K. In the following the high

212 temperature shoulder remains roughly at the same position for further addition of Pd,

213 stabilizing the observed liquidus temperature. Between 17.5 and 30 at% the peaks mainly

214 change their shape and position until they merge again at 35 at% Pd to a single main peak with

215 a distinct shoulder. This evolution of the shape of the peak is briefly summarized in SI Fig. 1.
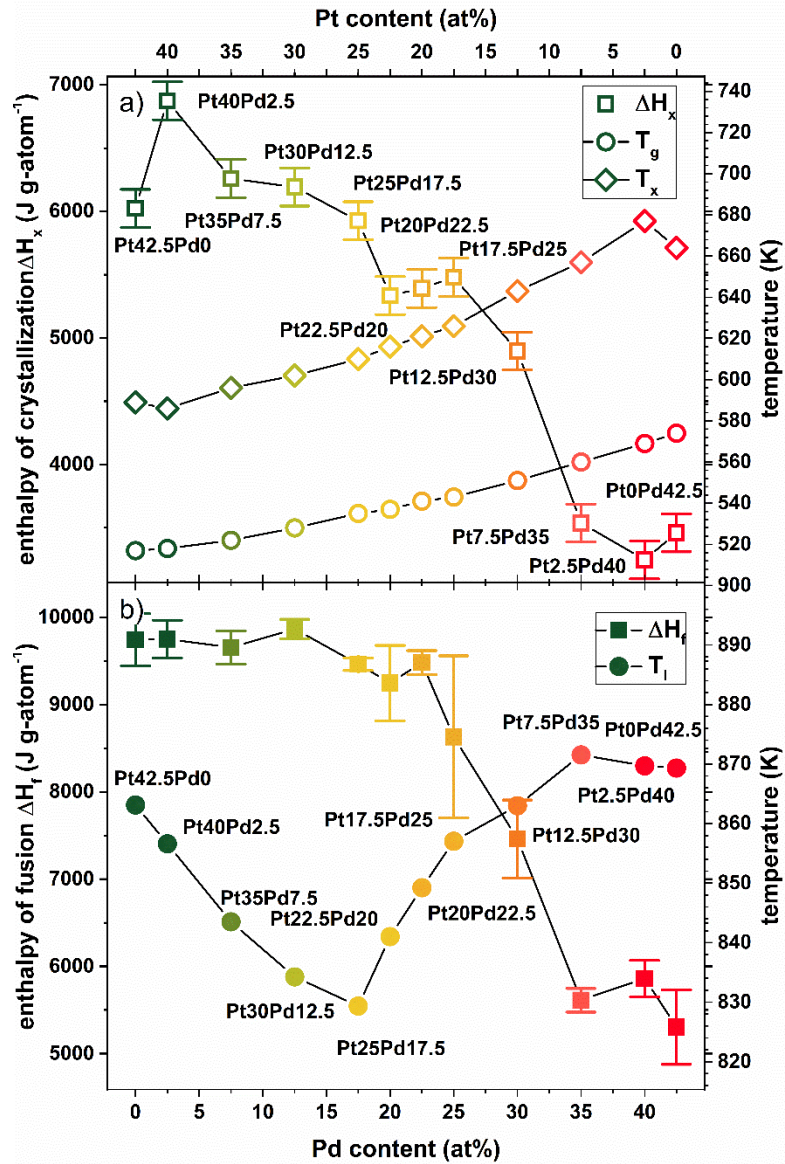
Figure 2: a) Results of the low temperature DSC measurements of the glass transition temperature (open circle) and the onset of crystallization (open diamonds) and the enthalpy of crystallization (open rectangle) of $Pt_{42.5-x}Pd_xCu_{27}Ni_{9.5}P_{21}$ as a function of Pd content at a heating rate of 0.33 Ks^{-1}

b) Results of high temperature DSC measurements including enthalpies of fusion (filled rectangle) and liquidus temperatures (filled circles)) of $Pt_{42.5-x}Pd_xCu_{27}Ni_{9.5}P_{21}$ as a function of Pd content at a heating rate of 0.33 Ks^{-1}. The decrease in ΔH_f reflects the changes in entropy of fusion ΔS_f, which is the slope of the difference in Gibbs free energy

225 **at the liquidus temperature $\Delta G^{l-x}(T_l)$. Error bars of glass transition, crystallization and**

226 **liquidus temperatures are in the size of the symbols and are therefore not shown.**

227

228 In contrast to the ongoing changes in shape, and magnitude of the melting peak, the enthalpy

229 of fusion, remains relatively stable at around 9.5 kJ g-atom^{-1} until an amount of 22.5 at% of Pd

230 is reached. From here a sudden drop to around 5.5 kJ g-atom^{-1} for alloys containing 35 at% or

231 more Pd is observed. This progression of the enthalpy of fusion with rising Pd content is very

232 similar to that observed for the enthalpy of crystallization, graphically summarized in Fig. 2a)

233 and b). Compared to the, close to linear, dependence of the glass-transition and crystallization

234 temperature the enthalpies rather show a sigmoidal trend, strictly shifting from "Pt-like" to

235 "Pd-like" behavior. Further it seems notable that most significant changes occur on the Pd-rich

236 side and not right in the middle of the compositional range. Further the *Pt25Pd17.5*

237 composition shows the minimum in the liquidus temperature as well as the smallest melting

238 interval T_l-T_m, i.e., the composition closest to eutectic behavior is located on the Pt-rich side.

239 for. Therefore, a possible change of the primary crystalline phases would rather be expected on

240 the Pt-rich side than in the middle.

241 A detailed summary on the characteristic temperatures and enthalpies of all examined alloys is

242 provided in Table 1. Here also the melting point of samples that are crystallized in the up-scan

243 of initially amorphous samples with 0.33 K s^{-1} is provided (for plot see SI Fig. 2). It shall be

244 noted that due to the occurrence of several metastable crystalline phases in the alloy system the

245 onset of melting is strongly depending on the thermal history/crystallization sequence (compare

246 SI Fig. 3), similar to observations in Au-based BMGs during fast scanning calorimetry

247 (FDSC) [26]. The narrowing of the temperature range of melting is further summarized in

248 SI Fig. 2, depicting the evolution of the melting and liquidus temperature.

13

249 **Table 1: Summary of characteristic temperatures and enthalpies extracted from DSC**

250 **scans at a heating rate of 0.33 K s^{-1} of X-ray amorphous samples.**

alloy	T_g (K)	T_x (K)	T_m (K)	T_l (K)	H_x (kJ g-atom^{-1})	ΔH_f (kJ g-atom^{-1}	ΔS_f (J g-atom^{-1}
Pt42.5Pd0	517	589	799	863 ± 0.4	6 ± 0.2	9.7 ± 0.3	11.3 ± 0.3
Pt40Pd2.5	518	586	799	857 ± 0.2	6.9 ± 0.2	9.8 ± 0.2	11.4 ± 0.3
Pt35Pd7.5	522	596	801	844 ± 0.2	6.3 ± 0.2	9.7 ± 0.2	11.4 ± 0.2
Pt30Pd12.5	528	602	803	834 ± 0.6	6.2 ± 0.2	9.9 ± 0.1	11.8 ± 0.1
Pt25Pd17.5	535	610	798	829 ± 0.4	5.9 ± 0.2	9.5 ± 0.1	11.4 ± 0.1
Pt22.5Pd20	537	616	786	841 ± 1.2	5.3 ± 0.2	9.3 ± 0.4	11 ± 0.5
Pt20Pd22.5	541	621	771	849 ± 0.9	5.4 ± 0.2	9.5 ± 0.1	11.2 ± 0.2
Pt17.5Pd25	543	626	777	857 ± 2.7	5.5 ± 0.2	8.6 ± 0.9	10.1 ± 1.1
Pt12.5Pd30	551	643	765	862 ± 2.4	4.9 ± 0.2	7.5 ± 0.5	8.6 ± 0.5
Pt7.5Pd35	560	657	778	872 ± 3.5	3.5 ± 0.2	5.6 ± 0.1	6.4 ± 0.2
Pt2.5Pd40	569	677	790	870 ± 0.9	3.3 ± 0.2	5.9 ± 0.2	6.7 ± 0.2
Pt0Pd42.5	574	664	795	869 ± 2.1	3.5 ± 0.2	5.3 ± 0.4	6.1 ± 0.5

251

3.2. Specific isobaric heat capacity
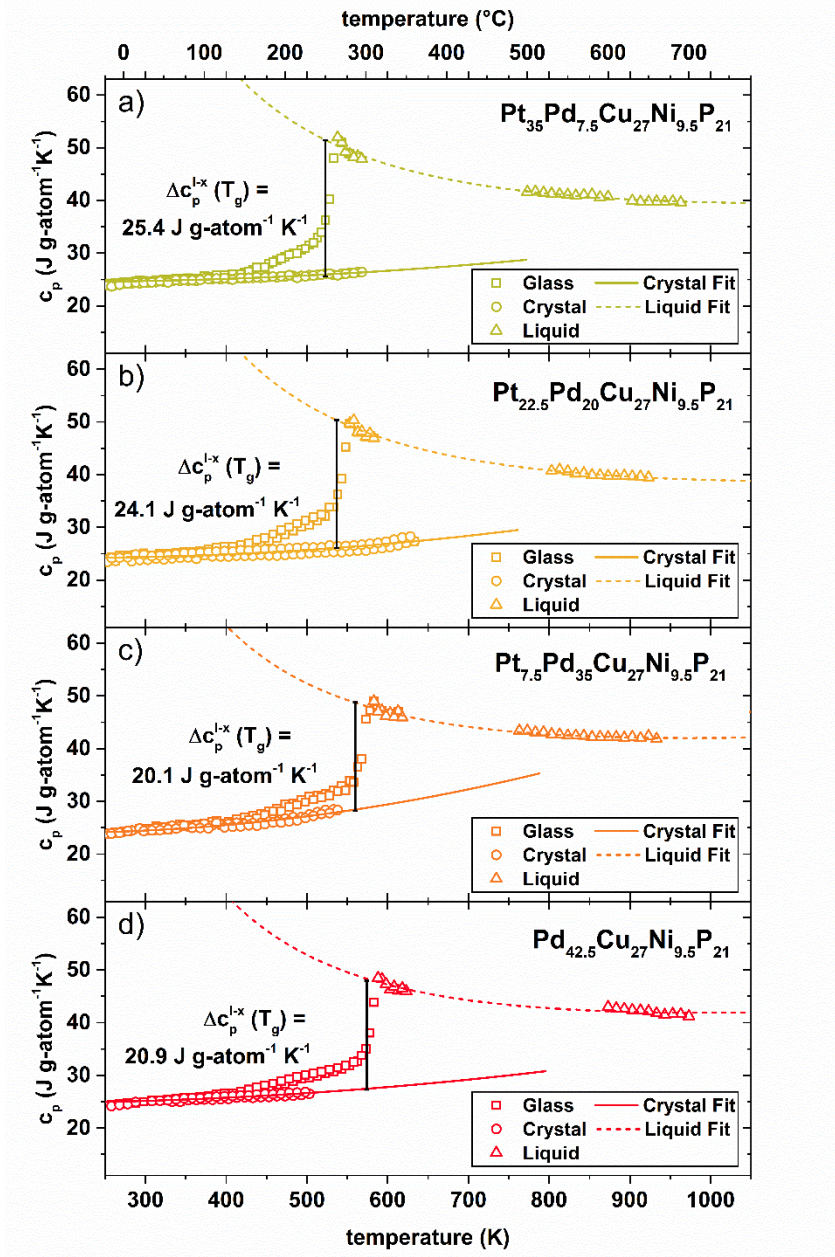
Figure 3: Specific isobaric heat capacity of glassy c_p (open rectangle), liquid (open triangle) and crystalline state (open circle) for $Pt_{35}Pd_{7.5}Cu_{27}Ni_{9.5}P_{21}$ (light green), $Pt_{22.5}Pd_{20}Cu_{27}Ni_{9.5}P_{21}$ (yellow), $Pt_{7.5}Pd_{35}Cu_{27}Ni_{9.5}P_{21}$ (orange) and $Pt_0Pd_{42.5}Cu_{27}Ni_{9.5}P_{21}$ (red). The fits of crystalline states (full line) and liquid states (dashed line) are based on the Kubaschewski equations, compare Eq. 1 and 2. Additionally, the difference in the specific isobaric heat capacity between liquid and crystalline state at the glass transition

15

temperature Δc_p^{l-x} (T_g) at a heating rate of 0.33 K/s is highlighted with a black bar for each alloy.

In Fig. 3a)-d) the specific heat capacity in glassy, (supercooled) liquid, equilibrium liquid and crystalline state, measured by a step-method with a sapphire standard, is exemplarily depicted for four different Pt/Pd ratios. For reasons of space and clarity only the data of these alloys is shown in this figure, while an overview of all twelve alloys is provided in the SI-Fig.4. Heat capacity data on the alloy *Pt42.5Pd0* was previously published in Ref. [10] The fits of the liquid (dashed line) and crystalline state (full line) are based on Eq. (1) and Eq. (2). The fitting parameters obtained for all twelve compositions are provided in Table 2. At low temperatures far away from the glass transition, but above the Debye-temperature, the specific heat capacity of the glassy and crystalline alloy are similar and at around 3 R ($\approx$25 J g-atom^{-1}K^{-1}) according to Dulong-Petits rule, typically observable in various metallic systems [17,27–29]. Independent of the glass transition temperature, the heat capacity of the glassy state begins to distinctively deviate from the crystal at around ~430 K, which can be traced back to relaxation effects. Here the assumption of a stable thermodynamic state is not fulfilled within the observation window. Therefore, it should be noted that the described specific heat capacities of the glass above ~430 K are unstable non-equilibrium values. This effect of relaxation becomes more eminent, when approaching the glass transition, where the glass fully relaxes to the supercooled liquid state. The respective jump in heat capacity at the glass transition temperature Δc_p^{l-x}(T_g(0.33 K s^{-1})) for a heating rate of 0.33 K s^{-1} is highlighted for each alloy. The lack of c_p-data between the deeply supercooled liquid and the liquidus temperature is caused by the limited thermal stability of the supercooled liquids and the resulting interference with crystallization.

283 **Table 2 Summary of the fitting parameters obtained by applying Eq. (1) and (2) to the**

284 **specific heat capacity data**

| alloy	$a \cdot 10^{-3}$ (J g-atom^{-1} K^{-2})	$b \cdot 10^{6}$ (J K g-atom^{-1})	$c \cdot 10^{-3}$ (J g-atom^{-1} K^{-2})	$d \cdot 10^{-6}$ (J g-atom^{-1} K^{-3})
Pt42.5Pd0	11.5852 ± 0.4865	5.1317 ± 0.1748	-7.2702 ± 0.4197	16.5269 ± 0.8654
Pt40Pd2.5	8.898 ± 0.3475	5.9989 ± 0.1148	-4.1856 ± 0.709	12.6481 ± 1.4416
Pt35Pd7.5	8.6865 ± 0.2238	6.0151 ± 0.085	-4.3478 ± 0.286	12.0134 ± 0.6025
Pt30Pd12.5	9.6033 ± 0.2109	5.9562 ± 0.0837	-4.2551 ± 0.9987	12.0506 ± 2.0343
Pt25Pd17.5	12.7526 ± 0.2683	5.3118 ± 0.0911	-5.0686 ± 0.8625	14.1399 ± 1.671
Pt22.5Pd20	7.968 ± 0.2362	6.0837 ± 0.0855	-7.0333 ± 0.8697	17.082 ± 1.6396
Pt20Pd22.5	9.6053 ± 0.1791	5.8765 ± 0.0712	-3.8779 ± 0.3081	11.6243 ± 0.6424
Pt17.5Pd25	15.5827 ± 0.2856	4.737 ± 0.1064	-5.2054 ± 0.2286	15.5093 ± 0.4592
Pt12.5Pd30	4.5858 ± 0.1466	6.8645 ± 0.0584	-9.0089 ± 0.3869	25.4256 ± 0.7216
Pt7.5Pd35	11.7029 ± 0.2488	5.3953 ± 0.0948	-10.6974 ± 1.0505	30.2484 ± 2.3118
Pt2.5Pd40	9.4793 ± 0.2841	5.908 ± 0.1153	-6.5437 ± 0.5034	21.6794 ± 0.9928
Pt0Pd42.5	11.4358 ± 0.2719	5.5529 ± 0.1101	-3.317 ± 0.851	13.4045 ± 1.9733

285
286
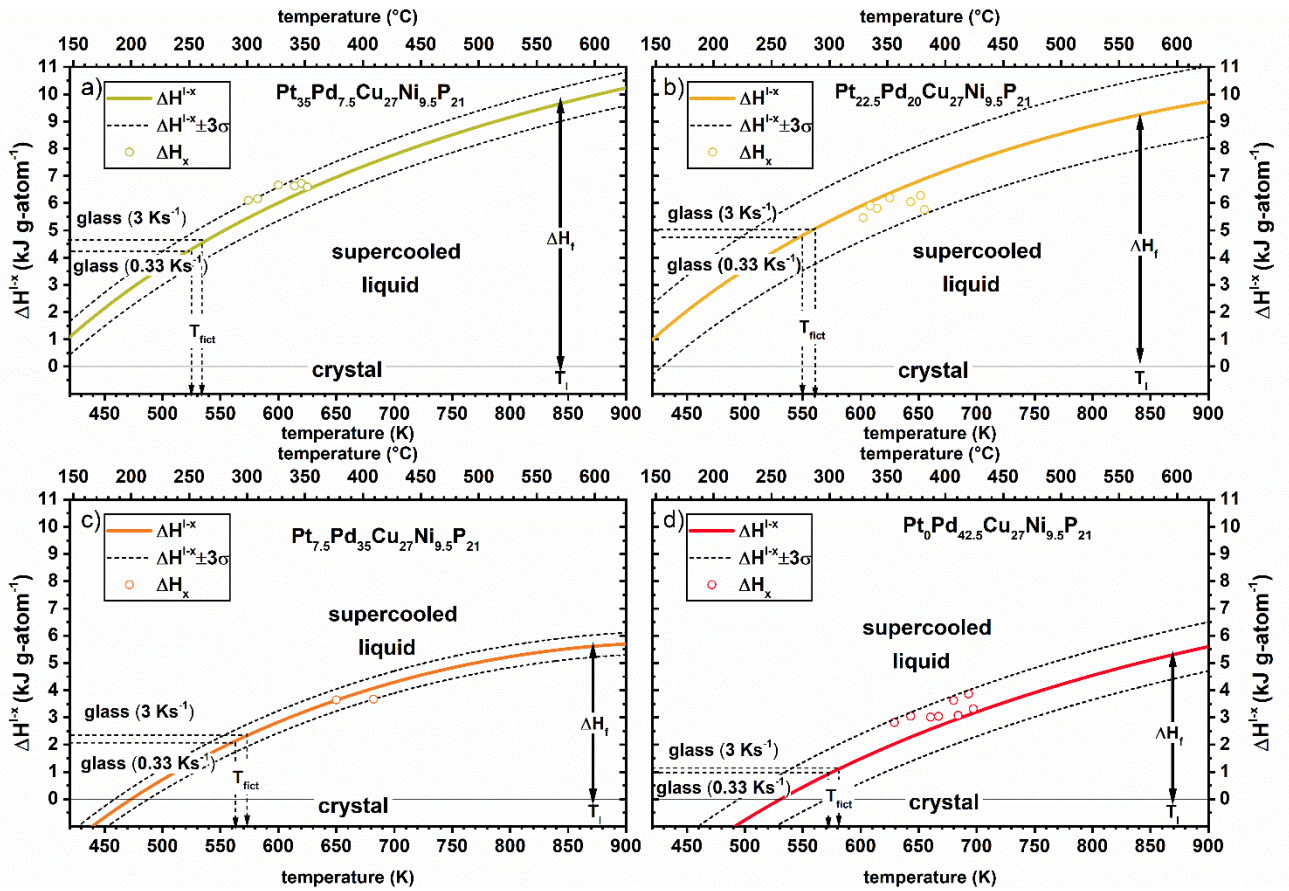
3.3. Enthalpy

Figure 4: Difference in excess enthalpy between liquid and crystalline state ΔH^{l-x}(T) for Pt$_{35}$Pd$_{7.5}$Cu$_{27}$Ni$_{9.5}$P$_{21}$ (light green), Pt$_{22.5}$Pd$_{20}$Cu$_{27}$Ni$_{9.5}$P$_{21}$ (yellow), Pt$_{7.5}$Pd$_{35}$Cu$_{27}$Ni$_{9.5}$P$_{21}$ (orange) and Pt$_{0}$Pd$_{42.5}$Cu$_{27}$Ni$_{9.5}$P$_{21}$ (red). A confidence interval of ± 3σ (dashed line) is depicted to account for experimental uncertainty and crystallization enthalpies (open circles) from independent DSC measurements are inserted to support the validity of the calculation of the enthalpic curves based on measurements of the specific isobaric heat capacity and enthalpies of fusion (compare Fig. 2 and Fig. 3). Further the residual enthalpies for two different cooling rates, based on the respective fictive temperature are shown for each alloy by horizontal dashed lines. It estimates the amount of enthalpy that is stored in a glass that has left the metastable liquid at the given cooling rate. Error bars of the crystallization enthalpies are in the size of the symbols and are therefore not shown.

18

300

301 The determined functions of the isobaric heat capacity of liquid and crystalline state allow a

302 description of the enthalpy during undercooling for all observed liquids with respect to the

303 crystalline state. The excess enthalpy between liquid and crystal $\Delta H^{l-x}(T)$ can be described by

304

305
$$\Delta H^{l-x}(T) = \Delta H_f + \int_{T_{fusion}}^{T} \Delta c_p^{l-x}(T')dT' \qquad (6),$$

306 with T_{fusion} being the temperature of fusion. The temperature of fusion defines the temperature

307 at which the difference in Gibbs free energy between crystal and liquid ΔG^{l-x} would become

308 zero. In this context the liquidus temperature is used as the temperature of fusion, presuming

309 thermodynamic equilibrium at this temperature. Since the present alloys do not show congruent

310 melting, attention must be put to this assumption. For very off-eutectic systems, especially

311 those showing a high temperature shoulder during melting, it can lead to underestimations of

312 the excess enthalpy. Nevertheless, T_l can be seen as a valid assumption, as it marks the first

313 temperature boundary, under which a driving force for (partial) crystallization is eminent in

314 multi-component systems.

315 In Fig. 4 the course of the excess enthalpies of the four exemplary alloys, already used in the

316 depiction of the heat capacity data, is shown. In addition to the $\Delta H^{l-x}(T)$ curves a

317 $\pm 3\sigma$ confidence interval, with σ being the standard deviation of the enthalpy of fusion, is

318 shown. For each alloy resulting crystallization enthalpies ΔH_x of non-isothermal crystallization

319 experiments at various rates between 0.025 K s^{-1} and 3 K s^{-1} are depicted. The variation of

320 heating rates leads to different crystallization temperatures, which due to the difference in heat

321 capacity Δc_p^{l-x} ultimately results in the different crystallization enthalpies, being consistent

322 with the enthalpy changes that are calculated from integrating the specific heat capacities.

323 At the low-temperature branch of each $\Delta H^{l-x}(T)$ curve horizontal lines are added to describe

324 the residual enthalpy ΔH_{res} ($\dot{T}$) of a glass that has initially left its metastable equilibrium at a

19

325   cooling rate $\dot{T} = dT/dt$ at the fictive temperature $T_{fict}(\dot{T})$ [30]. The fictive temperature T_{fict} is

326   defined as the temperature where the metastable equilibrium is left during cooling [30].

327     $\Delta H_{res} (T_{fict})$ is a measure of the stored enthalpy in the glass assuming no further relaxation

328   below T_{fict}. Hence, it is a first order approximation or upper limit, as in real systems relaxation

329   is always present in the wider surroundings of the glass transition region (compare to the heat

330   capacity of the glass in Fig. 3). The $\Delta H^{l-x}(T)$ curves of all twelve examined alloys can be found

331   in SI Fig. 5.

332

4. Discussion

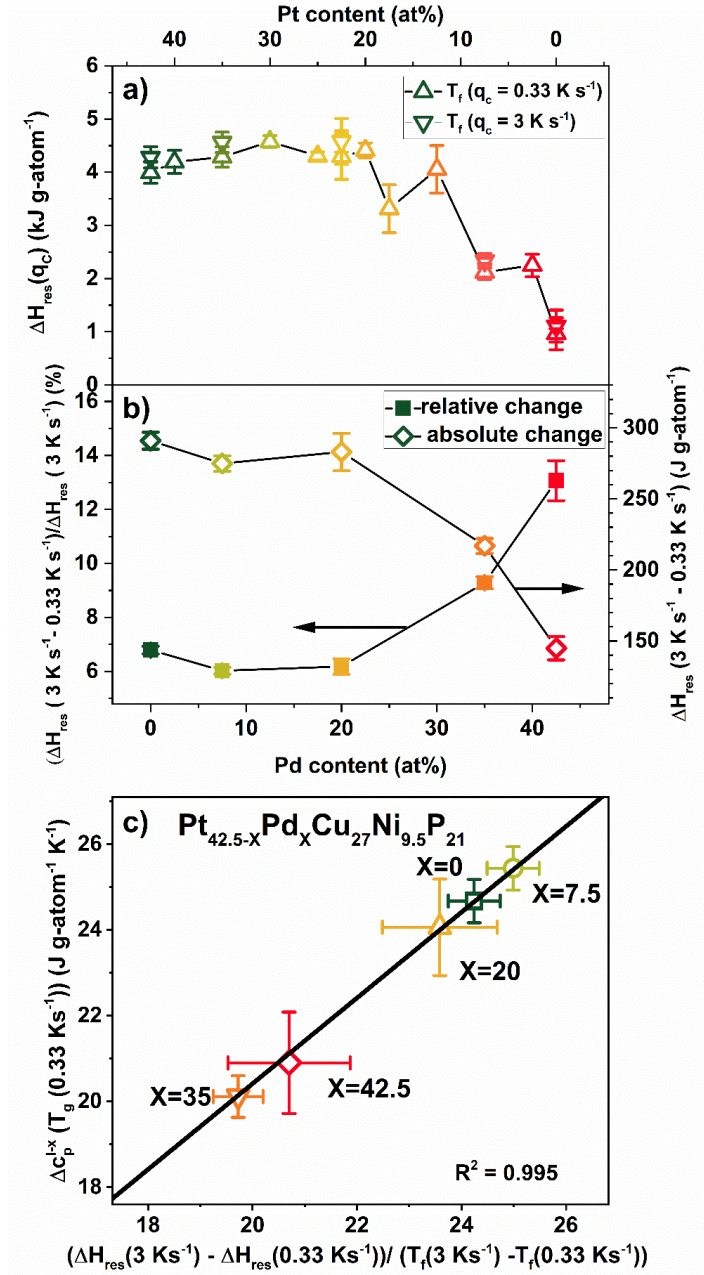### 4.1. Residual Enthalpy and connection to mechanic properties

Figure 5:a) Compositional dependence of the residual enthalpy that is frozen in at the glass transition temperature for the cooling rate of 0.33 K s⁻¹ (all alloys) and 3 K s⁻¹ (selected ones) with respect to the crystalline mixture. The residual enthalpy is calculated based on the excess enthalpy at the fictive temperature at the specific cooling rate $\Delta H^{l-x}(T_f) = \Delta H_{res}(T_f)$.

b) Compositional dependence of relative (left axis) and absolute (right axis) change of residual enthalpy ΔH_{res} between glasses created at 0.33 K s^{-1} and 3 K s^{-1}. The change in ΔH_{res} is a measure of the cooling-rate dependence of the enthalpy that is stored in the glass at a given cooling rate. Whereas in absolute numbers this change is the highest in Pt-rich alloys and very low in Pt0Pd42.5, the relative trend is the complete opposite. c) Scatter plot of the jump in specific heat capacity at the glass transition at a heating rate of 0.33 K s^{-1} over the difference in residual enthalpy between cooling rates of 0.33 K s^{-1} and 3 K s^{-1} normalized by the respective change in fictive temperature. A very good correlation of both parameters is found resulting with an $R^2 \geq 0.995$.

Due to their similar phenomenology, the descriptions of volume or enthalpy as a function of temperature are often used in synonymous ways in glass science. This inherent connection of volume and enthalpy for supercooled liquids and glasses was often pursued experimentally and good correlations for the relative changes of both quantities were shown for glasses in general [31] and in particular for metallic glasses [32–35]. Hence, knowledge of the excess residual enthalpy in the glass allows inferences about the excess volume that is trapped in the glassy state, called free volume [36]. Free volume is of high significance for the glassy state as it is connected to manifold properties e.g. diffusion, viscosity and especially plastic flow [37–39]. The plastic flow in metallic glasses can be understood as the local redistribution of the free volume through shear-transition zones (STZs) [39]. A large amount of free volume facilitates ductility as it allows for the activation of multiple shear bands, instead of a single shear band that fatally runs through the sample. Further it does facilitate the shielding of crack tips, as high free volume leads to a plastic zone that is composed of a high number of easy moving shear bands [40]. Thus, the ductility of the glass is inherently connected to the amount of free volume of the glass, which is governed by its thermal history and chemical composition [14,41,42].

365   Within this context predictions of the mechanical properties based on the enthalpy curves can

366   be made.

367   Regarding the mechanical properties Kumar et al. recently reported that Pt-based metallic

368   glasses show much higher plasticity than their Pd-based peers, connecting the Pd content to the

369   ductility [15]. Also structural considerations about the atomic connection schemes in Pt/Pd-

370   based metallic glasses by Gross et al supported/suggested the embrittlement through additional

371   Pd in these systems [13]. From our present results further predictions about the mechanical

372   properties can be derived by reviewing the residual enthalpies ΔH_{res} in the glassy state. In Fig.

373   5a) ΔH_{res} for a cooling rate of 0.33 K s^{-1} is shown as a function of Pd content. While the Pt-rich

374   alloys feature a very high amount of ΔH_{res} with around 4 kJ g-atom^{-1}, a sudden drop at 30 at%

375   Pd to about 2 or even 1 kJ g-atom^{-1} (*Pt0Pd42.5*) can be observed. Assuming the validity of the

376   proportionality of excess enthalpy and free volume [34], this leads to a higher amount of free

377   volume in the Pt-rich glasses in comparison to the Pd-based ones. This large amount of free

378   volume can ease the nucleation of multiple shear bands, facilitating plastic flow and ultimately

379   promote ductility for the alloys with large ΔH_{res}. Therefore, the enthalpy curves are in line with

380   the idea that Pd decreases the ductility in the Pt/Pd-Cu-Ni-P system by lowering its free volume.

381   It further agrees with the considerations regarding the mechanical properties based on structural

382   data by Gross et al [13]. Here changes of atomic connection schemes in the Pt/Pd-Cu-Ni-P

383   system were observed, suggesting a higher sensitivity towards embrittlement with rising Pd

384   content [13]. Now, based on ΔH_{res} as a function of Pd content, a first estimate of the location

385   of a ductile/brittle transition in compositional space can be made. Further does the sudden

386   decrease of ΔH_{res} at around 30 at% Pd, depicted in Fig. 5a), suggest a rather sudden drop than

387   a continuous decrease in the ductility, when consecutively replacing Pt by Pd in the alloys.

388   Nevertheless, the amount of ΔH_{res}, and hence the free volume does not only depend on the

389   composition, but also on the cooling rate. The cooling rate of the liquid defines, at which

390   temperature the metastable liquid is left (fictive temperature) and the glassy state is entered.

391   Ultimately, fast cooling rates end up in a higher fictive temperature and slower cooling rates

392   vice versa. The influence of the cooling rate on the ductility of a glass, described by the fictive

393   temperature of the glass, was briefly examined by Kumar et al. showing the existence of a so

394   called critical fictive temperature for embrittlement in different families of alloys [14]. In our

395   study a Pt-based system can be seen exemplary for a low, and a Pd based system for a high

396   critical fictive temperature, with respect to a standardized glass transition temperature.

397   Consequently, Pt can sustain much lower cooling rates than the Pd-based system and still

398   exhibit ductile behavior. From this the question arises if this cooling rate sensitivity is also

399   mirrored in the enthalpic scenario.

400   To account for the enthalpic changes due to the cooling rate the residual enthalpy at a cooling

401   rate of 3 K s^{-1}is also depicted in Fig. 5a) and the absolute and relative changes with respect to

402   a rate of 0.33 K s^{-1} are shown in Fig 5b). Regarding the absolute number, a steady decline of

403   the enthalpic changes can be seen with rising Pd content, reflecting the overall trajectory of the

404   residual enthalpy. It is a measure of the sensitivity of the residual enthalpy to different cooling

405   rates as well as to annealing. At a first glance, a larger change of the residual enthalpy would

406   mean a higher sensitivity to embrittlement. Although, as the total amount of residual

407   enthalpy/free volume should be decisive for the mechanical performance, a relative change of

408   ΔH_{res} might be a more representative measure of the cooling rate sensitivity towards

409   embrittlement. Regarding the relative changes to the residual enthalpy at 0.33 K s^{-1} the Pd

410   based glass shows a relative loss of 12% of its already low residual enthalpy, relating to its

411   higher sensitivity to embrittlement. Nevertheless, for the accurate way to quantify the

412   sensitivity to embrittlement of a glass, its critical fictive temperature or better the resulting

413   critical residual enthalpy/free volume, would have to be known. It would allow to scale the

414   enthalpic changes with this critical residual enthalpy, leading to the most physical way of

quantifying the cooling rate sensitivity. The values for the residual enthalpies are summarized in Table 3.

Further, the sensitivity to changes of the enthalpy with different cooling rates should depend on the specific heat capacity of the liquid and scale well with the difference in c_p of crystal and liquid at the glass transition. This means, the higher the step of c_p at T_g, the higher should be the c_p of the supercooled liquid and the larger should be the change in enthalpy with changing cooling rate and the more pronounced should be the cooling rate sensitivity of the ductility. When nominating the difference in residual enthalpy on the change of the fictive temperature for the two exemplary rates, which incorporates the kinetic behavior, a scatter plot shows a good correlation with $\Delta c_p^{l-x}(T_g)$ with an R^2 value of 0.995, depicted in Fig. 5c). The good correlation of both quantities is not surprising, as $\Delta H_{res}/\Delta T_{fict}$ is somehow a linear approximation, as c_p is defined as the first derivative of H with respect to temperature at constant pressure ($\partial H/\partial T|_{p=const}$). Nevertheless, since the enthalpic curve is based on the combination of heat capacity and independent measurements of the heat of fusion it is a validation of the calculations and the used assumptions. At this point it shall be noted that $\Delta c_p^{l-x}(T_g)$ is connected to the thermodynamic fragility, discussed in detail later, which underlines the possible role of fragility regarding the mechanical properties. The given considerations underline the possibility to estimate the cooling rate sensitivity of the residual enthalpy, based on heat capacity data. It shall be remarked that the correlation of cooling rate sensitivity to the c_p is only robust, when the fictive temperature is showing similar cooling rate dependencies, which means similar kinetic fragilities.

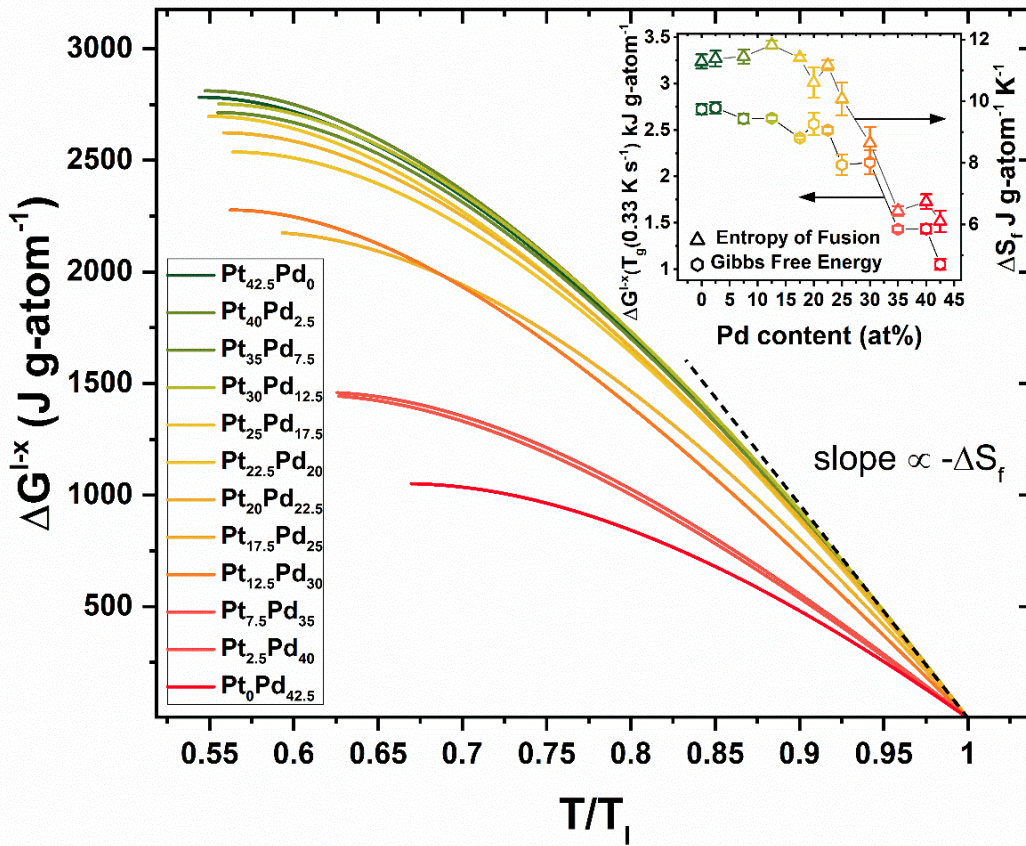## 4.2. Gibbs free energy and driving force for crystallization

Figure 6: Difference in Gibbs free energy between the supercooled liquid and the crystalline mixture ΔG^{l-x} for the Pt-Pd-Cu-Ni-P based bulk metallic glass-forming liquids over the by the liquidus temperature normalized temperature T/T_l. A consecutive decrease of the free energy curves with rising Pd-content is observed. The inset summarizes the value of the Gibbs free energy at the glass transition temperature for a cooling rate of 0.33 K s^{-1} ΔG^{l-x} (T_g(0.33 K s^{-1}) , being a lower estimate for the maximum in driving force for crystallization that the liquid experiences before leaving its thermodynamic equilibrium. In addition, the entropy in fusion ΔS_f is shown on the right axis of the inset, showing the same trend as the Gibbs free energy. A dashed line is added to the curves to underline that the value of ΔS_f marks the slope of $\Delta G^{l-x}(T_l)$.

449   Based on specific heat capacities and melting enthalpies a calculation of the difference in Gibbs

450   free energy between the liquid and crystalline mixture ΔG^{l-x} is possible with

451
$$\Delta G^{l-x}(T) = \Delta H^{l-x}(T) - T\,\Delta S^{l-x}(T), \tag{7}$$

452   and

453
$$\Delta S^{l-x}(T) = \Delta S_f + \int_{T_f}^{T} \frac{\Delta C_p^{l-x}(T')}{T'} dT', \tag{8}$$

454
$$\Delta S_f = \frac{\Delta H_f}{T_l}. \tag{9}$$

455

456   , where ΔS^{l-x} describes the excess entropy between liquid and crystalline state and ΔS_f is the

457   entropy of fusion. The difference in Gibbs free energy between liquid and crystalline state

458   allows a lower estimation of the driving force for crystallization in a multicomponent

459   system [43]. Therefore it can be used to describe the thermodynamic contribution to the

460   GFA of a liquid [2,3,44–46]. To relate it to the degree of undercooling ΔG^{l-x} is plotted as a

461   function of temperature normalized to the liquidus temperature in Fig. 6a.

462   A decrease of the difference in Gibbs free energy is observed with increasing Pd content. For

463   reasons of clarity a depiction of the Gibbs free energy at the glass transition temperature for

464   0.33 K s^{-1} (fictive temperature) together with the entropy of fusion ΔS_f, is provided in the inset.

465   For the total values of ΔS_f, the Pt-rich alloys trend to show a higher, whereas the Pd-rich alloys

466   feature a lower value than expected by Richard's rule, which predicts an approximated ΔS_f of

467   8.78 J g-atom^{-1}K^{-1} $\approx$ R for metals [47], while elemental Pd and Pt are both known to follow

468   Richards rule very well [47]. The entropy of fusion further represents the negative slope of the

469   ΔG^{l-x} ($\partial \Delta G^{l-x}/\partial T|_{T=Tl} = -\Delta S_f$) curves at the liquidus temperature. The compositional dependence

470   of ΔG^{l-x} is very similar to the changes of the enthalpy and entropy of fusion ΔS_f, in the system.

471   This good agreement was shown in several systems e.g. Au-based systems [48]. Therefore ΔS_f,

472   can be used as an estimation of ΔG^{l-x} (T) (Turnbull approximation) assuming a linear course of

473   ΔG^{l-x} (T) (physically relating to assumption of Δc_p^{l-x}=0) [49] with undercooling. The ΔG^{l-x} (T)

474   curves of *Pt42.5Pd0 and Pt0Pd42.5* are in good agreement to those reported for the same or

475   similar compositions *(*$Pd_{43}Cu_{27}Ni_{10}P_{20}$) in Refs. [12,50].

476   *Pt0Pd42.5* features one of the lowest driving forces for crystallization that was measured in

477   any metallic system and can therefore be considered a thermodynamically very stable liquid

478   against crystallization. Another parameter widely used to quantify the thermodynamic

479   contribution to GFA is the so called reduced glass transition temperature T_{rg}= T_g/T_l [51,52].

480   T_{rg} is a measure for the temperature range between the first occurrence of a driving force for

481   crystallization (here the liquidus temperature) and the moment of kinetic arrest (T_g). The

482   smaller this temperature span, which is critical for crystallization, the higher becomes T_{rg}.

483   Hence, the higher T_{rg}, the better should be the glass forming ability. The values of T_{rg}, provided

484   in Table 3 (also graphically depicted in SI Fig. 2), mirror the tendency of the driving forces

485   well. Still one has to note that here the change of T_{rg} is actually not caused by the change of

486   the liquidus temperature, as it is often observed [52], but rather by the increase of T_g with Pd

487   content. This suggests some changes of merely the liquid state. The additional Pd must

488   contribute to an internal slow-down of the liquid shifting the glass transition to higher

489   temperatures, without significantly influencing the liquidus temperature.

490   **Table 3: Summary of the thermodynamic characteristics derived from the isobaric heat**

491   **capacity data and melting analysis. The residual enthalpies are provided at fictive**

492   **temperatures of different cooling rates. If not particularly marked T_g values correspond**

493   **to a heating rate of 0.33 K s^{-1}.**

alloy	$\Delta c_p^{l-x}(T_g)$ (J g-atom^{-1} K^{-1})	$\Delta c_p^{l-x}/T_g$ (T_g) · 10$^-$	ΔH_{res}(0.33 K s^{-1}) (J g-atom^{-1})	ΔH_{res}(3 K s^{-1}) (J g-atom^{-1})	$\Delta G^{l-x}(T_g)$	T_{rg}

	$^3(J\ g\text{-}atom^{-1}\ K^{-2})$				$(J\ g\text{-}atom^{-1})$	
Pt42.5Pd0	24.7 ± 0.5	4.79 ± 0.1	3990 ± 80	4280 ± 90	2720 ± 60	0.599
Pt40Pd2.5	25.7 ± 0.6	4.97 ± 0.11	4190 ± 90	/	2740 ± 60	0.604
Pt35Pd7.5	25.4 ± 0.5	4.86 ± 0.1	4290 ± 90	4560 ± 90	2620 ± 50	0.618
Pt30Pd12.5	25.3 ± 0.3	4.8 ± 0.05	4580 ± 50	/	2630 ± 30	0.633
Pt25Pd17.5	24.1 ± 0.2	4.52 ± 0.04	4310 ± 30	/	2410 ± 20	0.645
Pt22.5Pd20	24.1 ± 1.1	4.46 ± 0.21	4300 ± 200	4580 ± 210	2560 ± 120	0.639
Pt20Pd22.5	24 ± 0.3	4.43 ± 0.06	4410 ± 60	/	2500 ± 40	0.637
Pt17.5Pd25	22.7 ± 1.2	4.18 ± 0.22	3310 ± 170	/	2120 ± 110	0.634
Pt12.5Pd30	22.1 ± 1.3	3.99 ± 0.24	4050 ± 240	/	2150 ± 130	0.639
Pt7.5Pd35	20.1 ± 0.5	3.58 ± 0.09	2120 ± 50	2340 ± 60	1430 ± 30	0.642
Pt2.5Pd40	20.3 ± 0.7	3.56 ± 0.13	2250 ± 80	/	1430 ± 50	0.654

| *Pt0Pd42.5* | 20.9 ± 1.2 | 3.64 ± 0.21 | 960 ± 50 | 1110 ± 60 | 1050 ± 60 | 0.660 |

494

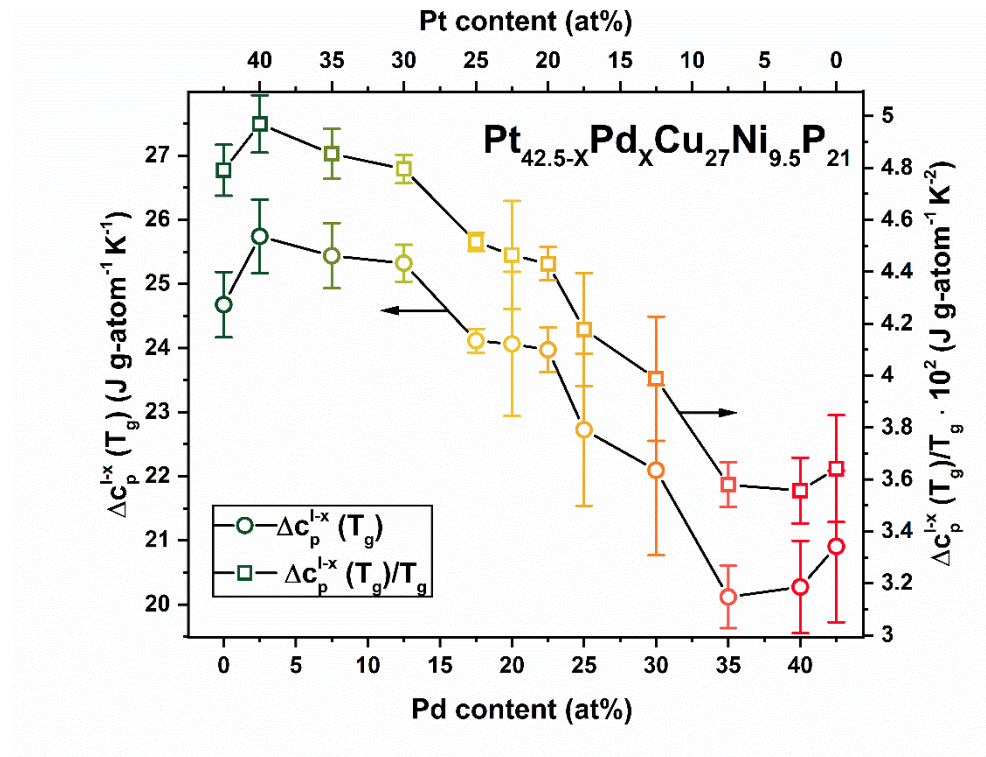## 4.3. Thermodynamic fragility and structural signatures

Figure 7 Difference in specific isobaric heat capacity between liquid and crystal Δc_p^{l-x} (T_g) as a function of Pd-content (left axis) together with the same difference being normalized by the glass transition temperature Δc_p^{l-x} (T_g)/T_g. This is a measure of the rate at which the configurational entropy of the liquid changes at the given temperature and ultimately reflects the thermodynamic fragility.

The rise of the glass transition temperature (Fig. 2, Tab. 1) within the alloy system already suggests a significant slowdown of the dynamics in the liquid state with rising Pd content. This leads to the question: Which thermodynamic property is the most appropriate to describe these changes? MD simulations suggest that structural redistribution and ordering processes of the deeply supercooled liquid lead to significant changes of the specific heat capacity with temperature close to the glass transition [53]. Therefore, the suggested dynamic slowdown of the liquid phase may also be reflected by the different temperature dependence of the specific

31

510 heat capacity of the liquid during cooling. This idea ultimately traces back to the theory of

511 Adam and Gibbs, assuming that the supercooled liquid is consisting of groups of atoms that

512 form so called cooperatively rearranging regions (CRRs). Upon undercooling the liquid, CRRs

513 grow in size and increase their degree of cooperativity. Hence, this process is consecutively

514 reducing the number of available configurations within the system [54], resulting in a decrease

515 of the configurational entropy S_c, accompanied by a rise of the specific heat capacity and being

516 connected to the tremendous rise of viscosity and relaxation times when approaching the glass

517 transition. In this framework Adam and Gibbs described the change in viscosity η, a

518 kinetic/dynamic quantity, using a temperature dependent thermodynamic quantity, the

519 configurational entropy $S_c(T)$ as

$$\eta(T) = \eta_0 \exp\left(\frac{C}{S_c(T)\,T} \right). \tag{10}$$

521 , where η_0 is the high temperature limit of viscosity and C is a constant that is proportional to

522 the free energy barrier for a cooperative rearrangement [55]. Under the assumption of a

523 neglectable difference in vibrational entropy between liquid and crystalline state,

524 experimentally underpinned by recent studies of Fultz et al. [56], the excess entropy ΔS^{l-x} can

525 be used instead of S_c to describe the entropic changes with temperature [57].

526 This connection between kinetic and thermodynamic properties allows to quantitatively

527 determine a thermodynamic fragility [50,58]. A connection between the excess entropy and the

528 kinetic fragility concept was qualitatively made by Angell and his co-workers as early as

529 2001 [57,59]. Instead of relaxation time or viscosity, the change of configurational

530 entropy/excess entropy around the glass transition is used to describe the (thermodynamic)

531 fragility.

532 Due to the connection of ΔS^{l-x} to Δc_p^{l-x} ($d\Delta S^{l-x}/dT = \Delta c_p^{l-x}/T$, compare equ. 8) and taking into

533 account the minor difference in the heat capacity of glass and crystal

534 ($\Delta c_p^{l-x}(T_g) \approx \Delta c_p^{l-g}(T_g)$) [60], the difference in specific isobaric heat capacity between liquid

535   and crystal $\Delta c_p^{l-x}(T_g)$ at the glass transition or rather the temperature nominated value

536     $\Delta c_p^{l-x}(T_g)/T_g \ (= d\Delta S^{l-x}/dT|_{T=T_g})$ can be used as a measure of thermodynamic fragility [50,57,58].

537   A larger c_p-step at the glass transition corresponds to a more rapidly increasing configurational

538   entropy in the liquid upon cooling, corresponding to thermodynamically more fragile behavior.

539   Vice versa, a smaller step is reflecting thermodynamically stronger behavior.

540   Both parameters $\Delta c_p^{l-x}(T_g)$ and $\Delta c_p^{l-x}(T_g)/T_g$, show the same development with changing Pt and

541   Pd content in Fig. 7, which is not surprising due to the linear progression of the glass transition

542   temperature with changing Pt/Pd ratio (compare Fig. 2a)). With growing Pd content the

543   increase of the heat capacity in the liquid state during cooling becomes shallower, i.e., the

544   decrease of excess entropy becomes smaller, which would be associated with a

545   thermodynamically stronger liquid behavior.

546   When reviewing the kinetic fragility in literature, fragility parameters D^* of 15.3 for

547   *Pt42.5Pd0* [10] and D^* values of 14.0 [11] for $Pd_{43}Cu_{27}Ni_{10}P_{20}$ are reported. This is surprising,

548   as both liquids should exhibit the thermodynamic signature of a similarly fragile metallic liquid.

549   However, the current results have drawn the different picture of a thermodynamically stronger

550   Pd-based liquid.

551   Nevertheless, the thermodynamically strong behavior agrees with the picture of the Pd-rich

552   liquid that is thermodynamically close to the crystalline state, as suggested by the Gibbs free

553   energy curves and the relatively low enthalpy and entropy of melting. This picture is further

554   supported by structural investigations by Gross et al. [13], which suggested the occurrence of

555   distinct structural motifs with different structural units and spatial arrangement in the Pt-P and

556   Pd-P liquids. Regarding the structural units, the Pt-P liquid contains a larger fraction of trigonal

557   prisms with a significant medium-range order (MRO), while the Pd-rich liquid features an

558   almost perfect icosahedral short-range order (SRO). Concerning the spatial arrangement, the

559   Pt-rich liquid shows a high diversity with 1-, 2- and even 4-atom connections of the individual

clusters, whereas the more rigid 3-atom connection seems to prevail for the Pd-rich liquid. This

high diversity of connection schemes of the structural units/clusters is further pointing towards

the high degree of medium range order in the Pt based system [13]. Ultimately it is assumed

that the thermodynamically strong behavior of the Pd rich alloys, deduced from the behavior

of the excess heat capacity and change of excess entropy, is in high resemblance to the

structural findings. Further it is hypothesized that the thermodynamic strong behavior is

presumably associated to the described variations in the distribution of cluster connections.
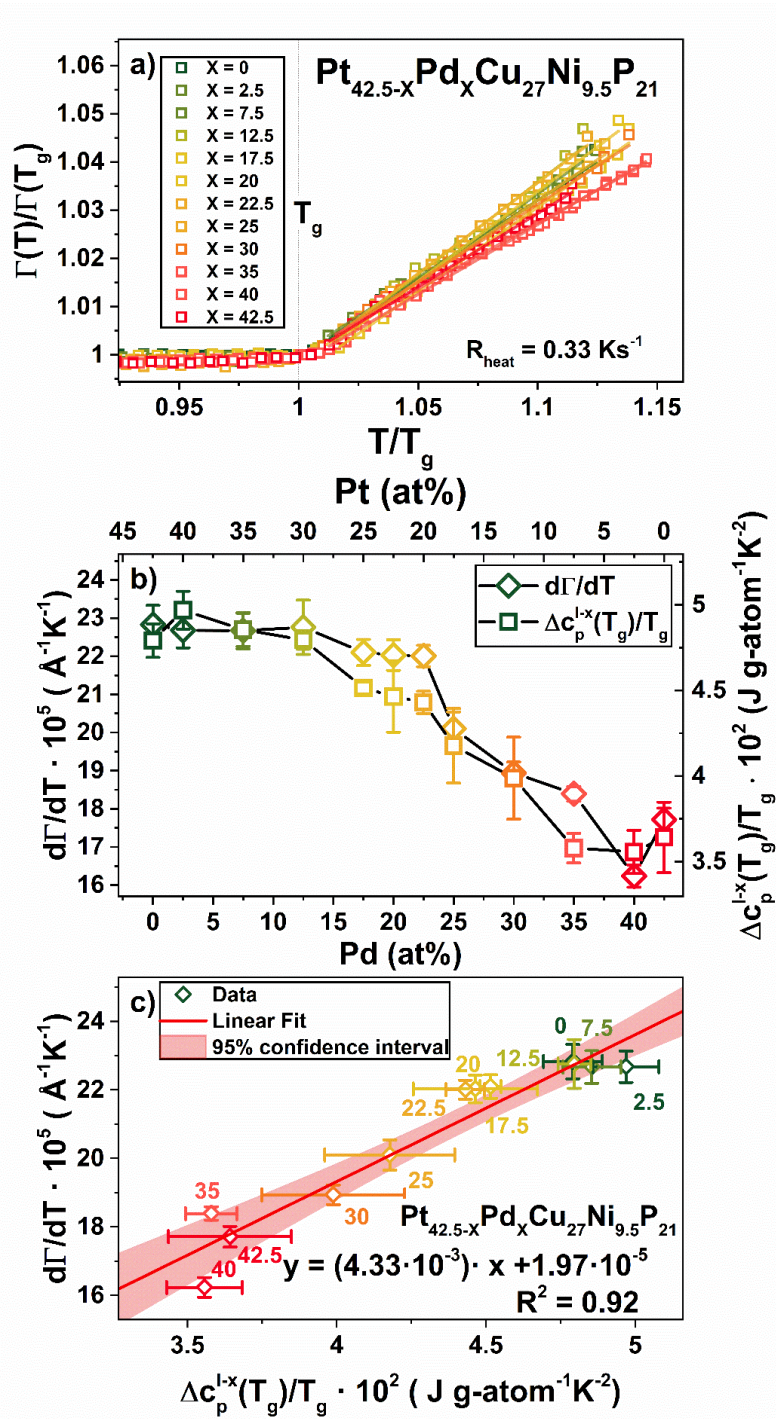
Figure 8: a) Full width half maximum (FWHM) $\Gamma(T)$ of the FSDP of the total structure factor S(Q) nominated on the FWHM at the respective glass transition temperature at 0.33 K s^{-1} $\Gamma(T_g)$ for all Pt/Pd variations on a T_g-normalized temperature scale. The measurements are carried out on samples that were priorly cooled with 0.33 K s^{-1} from the SCL state ($T_{g,end}$+10 K) to exclude structural relaxation during the main

measurement. Whereas the FWHM remains constant in the glassy region it shows a significant increase above the glass transition (here $T/T_g > 1$). A strong variation in the slope of the curves in the SCL with composition can be detected in the SCL region.

b) The change of FWHM of the FSDP of the total structure factor $S(Q)$ with temperature dT/dT in the SCL region as a function of Pd content (left axis) and the change of the difference in specific isobaric heat capacity between liquid and crystal nominated on the glass transition temperature $\Delta c_p^{l-x} (T_g)/T_g$ as a function of Pd content (right axis). Both quantities are showing the same trend in compositional space.

c) Scatter plot of the change in FWHM with temperature $d\Gamma/dT$ over the by T_g normalized difference in specific isobaric heat capacity between liquid and crystal $\Delta c_p^{l-x} (T_g)/T_g$. The latter describes the rate of loss of configurational entropy at the glass transition, ultimately being a measure of the thermodynamic fragility. A strong correlation of both quantities with an R^2-value of 0.92 was achieved, hinting towards at least a qualitative correlation within the system.

Following this argumentation, the evolution of the c_p-step at T_g and ultimately the thermodynamic fragility of the systems might be connected to the changes on the MRO length scale. In other words, the increasing c_p-step and slope of excess entropy upon substituting Pd by Pt might reflect the increasing diversity of cluster connection schemes. To structurally assess these relevant length-scales in X-ray diffraction experiments, the first sharp diffraction peak (FSDP) comprises a large part of the corresponding information [61]. Nevertheless, when connecting to macroscopic properties it is important to pay attention, as due to their large scattering cross-section [62], the scattering data is dominated by the contribution of Pt and Pd atoms. Hence, all structural information is merely reflecting the behavior of these large noble

596   metal atomic species, while the role of e.g., P cannot directly be probed by the used diffraction

597   techniques.

598   Especially with the focus on the characteristics of specific heat capacity and the change in

599   configurational entropy, the full width at half maximum (FWHM) Γ should be a good quantity

600   representing the diversity in the connection schemes, and therefore in the MRO. Structural

601   studies have shown that the FWHM of the FSDP correlates well with the correlation length

602   over which the period of a repeated unit survives, underlining its connection to the medium

603   range order in non-crystalline systems [63]. Further it was also used to characterize the

604   relaxation state and increasing MRO in a metallic glass [64]. The FWHM itself is very

605   sensitive to temperature changes and is broadening with increasing temperature due to the

606   increasing atomic vibrations (Debye-Waller factors [65]). The atomic clusters themselves are

607   representing the SRO of the system, whereas the interaction between the clusters and how they

608   are interconnected is described by the MRO. The change of the FWHM of the FSDP

609   corresponds to changes on the length scale of the MRO and therefore allow to quantify

610   differences in the cluster connections. A large temperature sensitivity of the FWHM of the

611   FSDP might resemble a high diversity of cluster connections (MRO) which should

612   thermodynamically condense in a larger change in configurational entropy, thus a

613   thermodynamically fragile behavior, as observed for the Pt-rich liquids.

614   For that reason, the FWHM Γ during heating is evaluated for the changing Pt/Pd content

615   throughout the glassy and SCL state until crystallization sets in. To exclude structural

616   relaxation effects during the heating, the samples were initially heated to a temperature

617    $T_{g,end}+10$ K and then cooled at the same rate of 0.33 K s^{-1} (see course of the FWHM in

618   SI Fig. 6). In Fig. 8a) the normalized FWHM is shown on a temperature scale normalized by

619   T_g. In the glassy state the FWHM features a shallow progression with temperature, leading to

620   a slope of almost zero. It is followed by an abrupt rise in FWHM, as the system is entering the

621   supercooled liquid state. Qualitatively the trend of the curves already shows high similarity to

622   the progression of excess enthalpy or entropy during heating from the glassy state, when

623   excluding relaxation effects. In the glassy state excess enthalpy and entropy are assumed to

624   remain frozen in/constant until reentering the (supercooled) liquid state, where significant

625   rearrangements, which can lead to enthalpic and entropic changes, are activated again. Above

626   the glass transition temperature different slopes of the FWHM are already visible by eye. While

627   the Pt-rich alloys feature a large increase of the peak width, this increase is less significant for

628   the liquids that feature higher Pd contents.

629   In Fig. 8b), the linearly fitted slope of the FWHM above the glass transition temperature with

630   respect to temperature, $d\Gamma/dT$, is depicted on the left axis, quantifying the graphical trend of

631   Fig. 8a), of a decreasing $d\Gamma/dT$ with rising Pd content. This means the temperature induced

632   changes in the peak width are becoming less prominent with increasing Pd content, well

633   mirroring the trend of $\Delta c_p^{l-x}(T_g)/T_g$, with Pd content, which is added on the right axis of Fig. 8b).

634   Considering $\Delta c_p^{l-x}(T_g)/T_g$ as a measure of the rate of change in excess entropy $\Delta S^{l-x}(T)$, the

635   tendency of a less pronounced ordering process of the liquid with rising Pd content, is

636   qualitatively mirrored by the smaller structural changes regarding the width of the FWHM.

637   Therefore, the structure of the Pd based systems are showing smaller temperature induced

638   changes, resembling a structurally stronger behavior compared to the Pt-rich systems.

639   Ultimately, the scatter plot of Fig. 8c) proves the good qualitative congruence between the

640   temperature induced changes of the FWHM $d\Gamma/dT$ and the changes in specific heat capacity at

641   the glass transition temperature $\Delta c_p^{l-x}(T_g)/T_g$., which in the end serves as a measure of the

642   thermodynamic fragility. Thus, it can be conjectured that the Pd based alloys behave

643   thermodynamically and structurally stronger than the Pt based liquids, which is also in

644   accordance with the findings based on the structural fragility concept of Wei et al. (compare

645   Ref. [66]) for the $Pt_{42.5}Cu_{27}Ni_{9.5}P_{21}$ and $Pd_{43}Cu_{27}Ni_{10}P_{20}$ liquid [11].

646 Although, both Pt- and Pd-P liquid families feature significant differences in their

647 thermodynamic properties, which are also being detectable by different structural signatures,

648 the fact that both systems behave kinetically fragile leads to the fundamental question of the

649 origin of the kinetic fragility and its underlying structural mechanisms in metallic liquids.

650 Consequently, the Pt/Pd-P based liquids appear to be the ideal candidate for further research

651 on the connection between thermodynamics, kinetics, and structure. To elucidate this

652 fundamental issue additional work will be needed to further examine the dynamic and kinetic

653 behavior of the Pd-rich liquids to shed light on their anomalous behavior. Especially methods

654 like X-ray photon correlation spectroscopy (XPCS), which enable the resolution of the

655 dynamics on the atomic scale, might be providing a new insight into the dynamics and kinetics

656 of these metallic systems and can possibly guide to a resolution of this dilemma.

657 **5. Conclusion**

658 In summary, the study reports on thermodynamic properties of the glassy, liquid and crystalline

659 phase of the Pt-Pd-Cu-Ni-P bulk metallic glass forming alloy system. The glass transition,

660 crystallization and melting event is assessed regarding characteristic temperatures and

661 enthalpies. Based on measurements of isobaric specific heat capacity, the alloy system is

662 thermodynamically modelled to calculate the enthalpic behavior of liquid and glassy state with

663 respect to the crystal and the driving forces for crystallization are estimated via calculations of

664 the Gibbs free energy difference between crystal and liquid.

665 The often suggested and, in an earlier study structurally indicated, scenario of rising tendencies

666 to embrittlement through Pd addition in the system was further underpinned through the

667 thermodynamic considerations. Via monitoring of the residual enthalpy in the glassy state as a

668 function of Pd content, a large amount of residual enthalpy was found for Pt-rich glasses

669 compared to their Pd-rich peers. Under the assumptions of a direct correlation of free volume

and residual enthalpy, the large free volume is assumed to facilitate multiple shear banding and ultimately promote ductility.

Furthermore, the Gibbs free energy curves of the liquid with respect to the crystalline state show a decreasing driving force for crystallization with increasing Pd content, resulting in an increasing thermodynamic stability of the liquid phase when replacing Pt with Pd. It systematically validates the surprisingly low driving force for similar Pd-based systems reported in literature.

Based on the behavior of the excess specific heat capacity with temperature, the change of the excess entropy around the glass transition was derived, suggesting a thermodynamically stronger behavior with increasing Pd content. This stands in a contrast to the reported kinetic fragilities, which would propose a constant or even more fragile behavior with growing Pd content. To resolve this discrepancy also the structural changes with temperature are examined with HEXRD. From this a good correlation between the excess heat capacity at the glass transition/rate of loss of configurational entropy with the change of the FWHM of the FSDP Γ in the liquid state with respect to temperature $d\Gamma/dT$ is found. This further supports the picture drawn by the heat capacity data of a thermodynamically more fragile Pt system, that is undergoing more severe structural changes on the length scale of the FSDP during cooling and the rather strong Pd system that remains comparably stable/unchanged on these observed length scales. Finally, the findings can be seen as another milestone in the understanding of structural changes on the MRO length scale and their connection to thermodynamic parameters, such as excess heat capacity or configurational entropy, and ultimately thermodynamic fragility.

692

700

7. References

[1]   C.A. Angell, Formation of glasses from liquids and biopolymers, Science (80-.). 267 (1995) 1924–1935. https://doi.org/10.1002/hlca.19690520729.

[2]   W.H. Busch, R.; Schroers, J.; Wang, T hermodynamics and Kinetics of Bulk Metallic Glass Thermodynamics of Supercooled, MRS Bull. 32 (2007) 620–623.

[3]   R. Busch, The Thermophysical Properties of Bulk Metallic Glass-Forming Liquids, (2000) 39–42.

[4]   R.W. Cahn, P. Haasen, E.J. Kramer, Glasses and amorphous materials, Mater. Sci. Technol. 9 (1991) 493.

[5]   D.B. Miracle, A structural model for metallic glasses, Microsc. Microanal. 10 (2004) 786–787. https://doi.org/10.1038/nmat1219.

[6]   D.B. Miracle, The efficient cluster packing model - An atomic structural model for metallic glasses, Acta Mater. 54 (2006) 4317–4336. https://doi.org/10.1016/j.actamat.2006.06.002.

[7]   K.J. Laws, D.B. Miracle, M. Ferry, A predictive structural model for bulk metallic glasses, Nat. Commun. 6 (2015) 1–10. https://doi.org/10.1038/ncomms9123.

[8]   N. Nishiyama, K. Takenaka, H. Miura, N. Saidoh, Y. Zeng, A. Inoue, The world's biggest glassy alloy ever made, Intermetallics. 30 (2012) 19–24.

[9]   J. Schroers, W.L. Johnson, Highly processable bulk metallic glass-forming alloys in the Pt-Co-Ni-Cu-P system, Appl. Phys. Lett. 84 (2004) 3666–3668. https://doi.org/10.1063/1.1738945.

[10]   O. Gross, B. Bochtler, M. Stolpe, S. Hechler, W. Hembree, R. Busch, I. Gallino, The kinetic fragility of Pt-P- and Ni-P-based bulk glass-forming liquids and its thermodynamic and structural signature, Acta Mater. 132 (2017) 118–127. https://doi.org/10.1016/j.actamat.2017.04.030.

[11]   O. Gross, Precious metal based bulk glass-forming liquids: Development, thermodynamics, kinetics and structure, Diss. Saarl. Univ. (2018). https://doi.org/10.22028/D291-27993.

[12]   O. Gross, S.S. Riegler, M. Stolpe, B. Bochtler, A. Kuball, S. Hechler, R. Busch, I. Gallino, On the high glass-forming ability of Pt-Cu-Ni/Co-P-based liquids, Acta Mater. 141 (2017) 109–119. https://doi.org/10.1016/j.actamat.2017.09.013.

[13]   O. Gross, N. Neuber, A. Kuball, B. Bochtler, S. Hechler, M. Frey, R. Busch, Signatures of structural differences in Pt–P- and Pd–P-based bulk glass-forming liquids, Commun. Phys. 2 (2019) 83. https://doi.org/10.1038/s42005-019-0180-2.

[14]   G. Kumar, P. Neibecker, Y.H. Liu, J. Schroers, Critical fictive temperature for plasticity in metallic glasses, Nat. Commun. 4 (2013) 1536. https://doi.org/10.1038/ncomms2546.

[15]   G. Kumar, S. Prades-Rodel, A. Blatter, J. Schroers, Unusual brittle behavior of Pd-based bulk metallic glass, Scr. Mater. 65 (2011) 585–587. https://doi.org/10.1016/j.scriptamat.2011.06.029.

[16]   L. Sun, Q. Wu, Y. Xu, W. Wang, Study on solidification behaviour of Pd40Ni40P20 alloy by fluxing method, Phys. B Condens. Matter. 240 (1997) 205–210.

[17]   R. Busch, W. Liu, W.L. Johnson, Thermodynamics and kinetics of the Mg65Cu25Y10bulk metallic glass forming liquid, J. Appl. Phys. 83 (1998) 4134–4141. https://doi.org/10.1063/1.367167.

[18]   B.A. Legg, J. Schroers, R. Busch, Thermodynamics, kinetics, and crystallization of Pt57.3Cu14.6Ni5.3P22.8 bulk metallic glass, Acta Mater. 55 (2007) 1109–1116. https://doi.org/10.1016/j.actamat.2006.09.024.

[19]   O. Kubaschewski, C.B. Alcock, P.J. Spencer, Materials thermochemistry, (1993) 363.

750   https://doi.org/10.2170/physiolsci.RP009208.

751   [20] A.C. Dippel, H.P. Liermann, J.T. Delitz, P. Walter, H. Schulte-Schrepping, O.H.
752   Seeck, H. Franz, Beamline P02.1 at PETRA III for high-resolution and high-energy
753   powder diffraction, J. Synchrotron Radiat. 22 (2015) 675–687.
754   https://doi.org/10.1107/S1600577515002222.

755   [21] A. Hammersley, Fit2d: an introduction and overview, Eur. Sychrotron Radi Facil. Int.
756   Rep. ESRF97HA02T. 68 (1997).

757   [22] X. Qiu, J.W. Thompson, S.J.L. Billinge, PDFgetX2: A GUI-driven program to obtain
758   the pair distribution function from X-ray powder diffraction data, J. Appl. Crystallogr.
759   37 (2004) 678. https://doi.org/10.1107/S0021889804011744.

760   [23] T. Egami, S.J.L. Billinge, UNDERNEATH THE BRAGG PEAKS Structural Analysis
761   of Complex Materials, 2nd ed., 2012.

762   [24] T.E. Faber, J.M. Ziman, A theory of the electrical properties of liquid metals, Philos.
763   Mag. 11 (1965) 153–173. https://doi.org/10.1080/14786436508211931.

764   [25] S. Wei, M. Stolpe, O. Gross, W. Hembree, S. Hechler, J. Bednarcik, R. Busch, P.
765   Lucas, Structural evolution on medium-range-order during the fragile-strong transition
766   in Ge15Te85, Acta Mater. 129 (2017) 259–267.
767   https://doi.org/10.1016/j.actamat.2017.02.055.

768   [26] S. Pogatscher, D. Leutenegger, J.E.K. Schawe, P.J. Uggowitzer, J.F. Löffler, Solid-
769   solid phase transitions via melting in metals, Nat. Commun. 7 (2016) 1–6.
770   https://doi.org/10.1038/ncomms11113.

771   [27] M. Frey, R. Busch, W. Possart, I. Gallino, On the thermodynamics, kinetics, and sub-
772   Tg relaxations of Mg-based bulk metallic glasses, Acta Mater. 155 (2018) 117–127.
773   https://doi.org/10.1016/j.actamat.2018.05.063.

774   [28] N. Neuber, O. Gross, M. Eisenbart, A. Heiss, U.E. Klotz, J.P. Best, M.N. Polyakov, J.
775   Michler, R. Busch, I. Gallino, The role of Ga addition on the thermodynamics,
776   kinetics, and tarnishing properties of the Au-Ag-Pd-Cu-Si bulk metallic glass forming
777   system, Acta Mater. 165 (2019) 315–326.
778   https://doi.org/10.1016/j.actamat.2018.11.052.

779   [29] A. Kuball, O. Gross, B. Bochtler, R. Busch, Sulfur-bearing metallic glasses: A new
780   family of bulk glass-forming alloys, Scr. Mater. 146 (2018) 73–76.
781   https://doi.org/10.1016/j.scriptamat.2017.11.011.

782   [30] C.T. MOYNIHAN, A.J. EASTEAL, M.A. De BOLT, J. TUCKER, Dependence of the
783   Fictive Temperature of Glass on Cooling Rate, J. Am. Ceram. Soc. 59 (1976) 12–16.
784   https://doi.org/10.1111/j.1151-2916.1976.tb09376.x.

785   [31] A. van den Beukel, J. Sietsma, The glass transition as a free volume related kinetic
786   phenomenon, Acta Metall. Mater. 38 (1990) 383–389. https://doi.org/10.1016/0956-
787   7151(90)90142-4.

788   [32] Z. Evenson, R. Busch, Equilibrium viscosity, enthalpy recovery and free volume
789   relaxation in a Zr44Ti11Ni10Cu10Be25 bulk metallic glass, Acta Mater. 59 (2011)
790   4404–4415. https://doi.org/10.1016/j.actamat.2011.03.064.

791   [33] A. Slipenyuk, J. Eckert, Correlation between enthalpy change and free volume
792   reduction during structural relaxation of Zr55Cu30Al10Ni 5 metallic glass, Scr. Mater.
793   50 (2004) 39–44. https://doi.org/10.1016/j.scriptamat.2003.09.038.

794   [34] O. Haruyama, Y. Nakayama, R. Wada, H. Tokunaga, J. Okada, T. Ishikawa, Y.
795   Yokoyama, Volume and enthalpy relaxation in Zr55Cu30Ni5Al10 bulk metallic glass,
796   Acta Mater. 58 (2010) 1829–1836. https://doi.org/10.1016/j.actamat.2009.11.025.

797   [35] M.E. Launey, J.J. Kruzic, C. Li, R. Busch, Quantification of free volume differences in
798   a Zr 44Ti 11Ni 10Cu 10Be 25bulk amorphous alloy, Appl. Phys. Lett. 91 (2007) 8–11.
799   https://doi.org/10.1063/1.2766659.

[36] D. Turnbull, M.H. Cohen, Free-volume model of the amorphous phase: Glass transition, J. Chem. Phys. 34 (1961) 120–125. https://doi.org/10.1063/1.1731549.

[37] G. Ruitenberg, P. De Hey, F. Sommer, J. Sietsma, Pressure dependence of the free volume in amorphous Pd40Ni40P20 and its implications for the diffusion process, Mater. Sci. Eng. A. 226–228 (1997) 397–400. https://doi.org/10.1016/s0921-5093(96)10651-1.

[38] W.L. Johnson, J. Lu, M.D. Demetriou, Deformation and flow in bulk metallic glasses and deeply undercooled glass forming liquids - A self consistent dynamic free volume model, Intermetallics. 10 (2002) 1039–1046. https://doi.org/10.1016/S0966-9795(02)00160-7.

[39] C.A. Schuh, T.C. Hufnagel, U. Ramamurty, Mechanical behavior of amorphous alloys, Acta Mater. 55 (2007) 4067–4109. https://doi.org/10.1016/j.actamat.2007.01.052.

[40] M.E. Launey, R. Busch, J.J. Kruzic, Effects of free volume changes and residual stresses on the fatigue and fracture behavior of a Zr-Ti-Ni-Cu-Be bulk metallic glass, Acta Mater. 56 (2008) 500–510. https://doi.org/10.1016/j.actamat.2007.10.007.

[41] A.R. Yavari, Absence of thermal embrittlement in some FeB and FeSiB glassy alloys, Mater. Sci. Eng. 98 (1988) 491–493. https://doi.org/10.1016/0025-5416(88)90214-5.

[42] T.W. Wu, F. Spaepen, The relation between enbrittlement and structural relaxation of an amorphous metal, Philos. Mag. B Phys. Condens. Matter; Stat. Mech. Electron. Opt. Magn. Prop. 61 (1990) 739–750. https://doi.org/10.1080/13642819008219307.

[43] Z. Evenson, On the thermodynamic and kinetic properties of bulk glass forming metallic systems, Univ. Des Saarlandes. (2012). https://doi.org/doi:10.22028/D291-22851.

[44] R. Busch, E. Bakke, W.L. Johnson, On the Glass Forming Ability of Bulk Metallic Glasses, Mater. Sci. Forum. 235–238 (1997) 327–336. https://doi.org/10.4028/www.scientific.net/MSF.235-238.327.

[45] H.-R. Jiang, B. Bochtler, S.S. Riegler, X.-S. Wei, N. Neuber, M. Frey, I. Gallino, R. Busch, J. Shen, Thermodynamic and kinetic studies of the Cu–Zr–Al(–Sn) bulk metallic glass-forming system, J. Alloys Compd. (2020) 156126. https://doi.org/10.1016/j.jallcom.2020.156126.

[46] M. Frey, R. Busch, W. Possart, I. Gallino, On the thermodynamics, kinetics, and sub-T_g relaxations of Mg-based bulk metallic glasses, Acta Mater. 155 (2018) 117–127. https://doi.org/10.1016/j.actamat.2018.05.063.

[47] J.W. Richards, Relations between the melting points and the latent heats of fusion of the metals, J. Franklin Inst. 143 (1897) 379–383. https://doi.org/10.1016/s0016-0032(97)90124-1.

[48] O. Gross, M. Eisenbart, L.Y. Schmitt, N. Neuber, L. Ciftci, U.E. Klotz, R. Busch, I. Gallino, Development of novel 18-karat, premium-white gold bulk metallic glasses with improved tarnishing resistance, Mater. Des. 140 (2018) 495–504. https://doi.org/10.1016/j.matdes.2017.12.007.

[49] D. Turnbull, Formation of crystal nuclei in liquid metals, J. Appl. Phys. 21 (1950) 1022–1028. https://doi.org/10.1063/1.1699435.

[50] I. Gallino, J. Schroers, R. Busch, Kinetic and thermodynamic studies of the fragility of bulk metallic glass forming liquids, J. Appl. Phys. 108 (2010) 063501. https://doi.org/10.1063/1.3480805.

[51] D. Turnbull, Under What Conditions Can A Glass Be Formed?, Contemp. Phys. 10 (1969) 473–488. https://doi.org/10.1080/00107516908204405.

[52] Z.P. Lu, H. Tan, Y. Li, S.C. Ng, Correlation between reduced glass transition temperature and glass forming ability of bulk metallic glasses, Scr. Mater. 42 (2000) 667–673. https://doi.org/10.1016/S1359-6462(99)00417-0.

850 [53] J. Ding, Y.Q. Cheng, H. Sheng, E. Ma, Short-range structural signature of excess
851   specific heat and fragility of metallic-glass-forming supercooled liquids, Phys. Rev. B
852   - Condens. Matter Mater. Phys. 85 (2012) 1–5.
853   https://doi.org/10.1103/PhysRevB.85.060201.
854 [54] P.G. Debenedetti, Metastable liquids: concepts and principles, Princeton university
855   press, 1996.
856 [55] G. Adam, J.H. Gibbs, On the temperature dependence of cooperative relaxation
857   properties in glass-forming liquids, J. Chem. Phys. 43 (1965) 139–146.
858   https://doi.org/10.1063/1.1696442.
859 [56] H.L. Smith, C.W. Li, A. Hoff, G.R. Garrett, D.S. Kim, F.C. Yang, M.S. Lucas, T.
860   Swan-Wood, J.Y.Y. Lin, M.B. Stone, D.L. Abernathy, M.D. Demetriou, B. Fultz,
861   Separating the configurational and vibrational entropy contributions in metallic
862   glasses, Nat. Phys. 13 (2017) 900–905. https://doi.org/10.1038/nphys4142.
863 [57] C.A. Angell, L.-M. Martinez, A thermodynamic connection to the fragility of glass-
864   forming liquids, Nature. 410 (2001) 663–667.
865 [58] I. Gallino, On the fragility of bulk metallic glass forming liquids, Entropy. 19 (2017).
866   https://doi.org/10.3390/e19090483.
867 [59] J. Ding, Y.Q. Cheng, H. Sheng, E. Ma, C.A. Angell, L.-M. Martinez, A
868   thermodynamic connection to the fragility of glass-forming liquids, Phys. Rev. B -
869   Condens. Matter Mater. Phys. 85 (2012) 1–5.
870   https://doi.org/10.1103/PhysRevB.85.060201.
871 [60] I. Gallino, O. Gross, G. Dalla Fontana, Z. Evenson, R. Busch, On the kinetic and
872   thermodynamic fragility of the Pt60Cu16Co2P22 and Pt57.3Cu14.6Ni5.3P22.8 bulk
873   metallic glasses, J. Alloys Compd. 615 (2015) S35–S39.
874   https://doi.org/10.1016/j.jallcom.2013.12.006.
875 [61] D. Ma, A.D. Stoica, X.L. Wang, Power-law scaling and fractal nature of medium-
876   range order in metallic glasses, Nat. Mater. 8 (2009) 30–34.
877   https://doi.org/10.1038/nmat2340.
878 [62] P.J. Brown, A.G. Fox, E.N. Maslen, M.A. O'Keefe, B.T.M. Willis, Intensity of
879   diffracted intensities, Int. Tables Crystallogr. C (2006) 554–595.
880   https://doi.org/10.1107/97809553602060000600.
881 [63] A.P. Sokolov, A. Kisliuk, M. Soltwisch, D. Quitmann, Medium-range order in glasses:
882   Comparison of Raman and diffraction measurements, Phys. Rev. Lett. 69 (1992)
883   1540–1543. https://doi.org/10.1103/PhysRevLett.69.1540.
884 [64] V.M. Giordano, B. Ruta, Unveiling the structural arrangements responsible for the
885   atomic dynamics in metallic glasses during physical aging, Nat. Commun. 7 (2016).
886   https://doi.org/10.1038/ncomms10344.
887 [65] I. Waller, Zur Frage der Einwirkung der Wärmebewegung auf die Interferenz von
888   Röntgenstrahlen, Zeitschrift Für Phys. 17 (1923) 398–408.
889 [66] S. Wei, M. Stolpe, O. Gross, Z. Evenson, I. Gallino, W. Hembree, J. Bednarcik, J.J.
890   Kruzic, R. Busch, Linking structure to fragility in bulk metallic glass-forming liquids,
891   Appl. Phys. Lett. 106 (2015) 10–15. https://doi.org/10.1063/1.4919590.
892
893

Supplementary Information

895

896
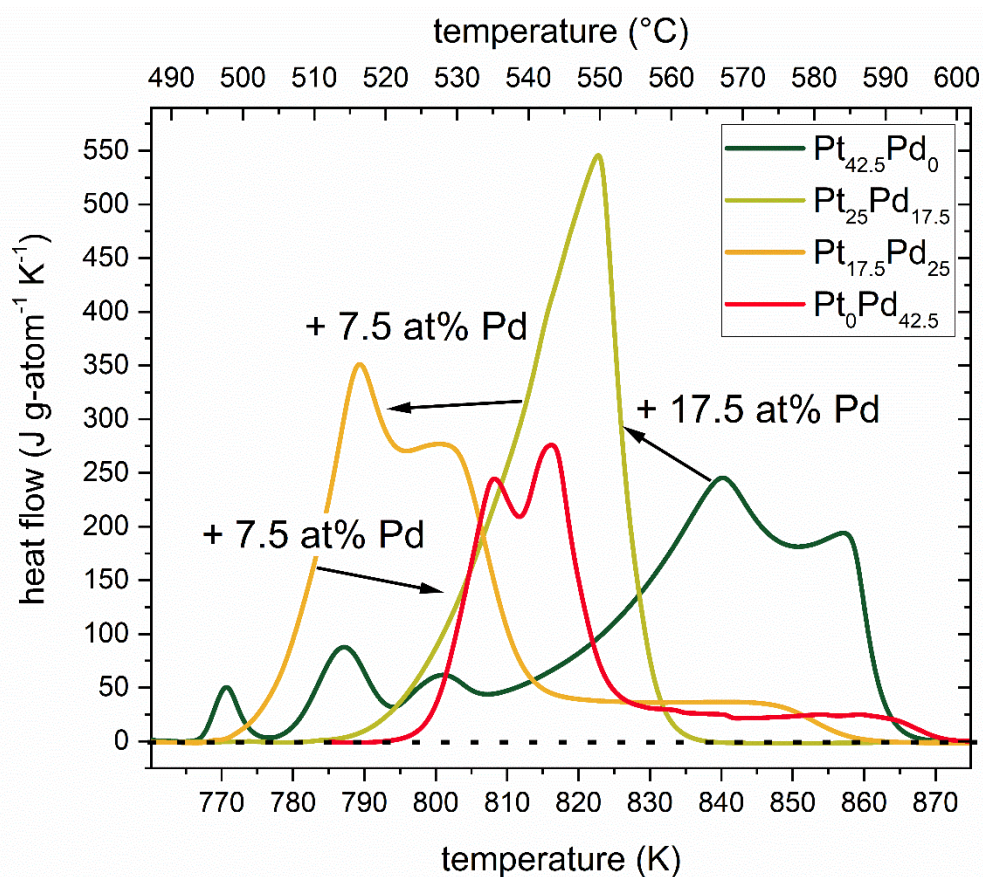
SI Figure 1: Evolution of the melting peak in $Pt_{42.5-x}Pd_xCu_{27}Ni_{9.5}P_{21}$ with Pd content. The respective changes in Pd content between each alloy are highlighted by arrows. First the melting peak is narrowing during the addition of Pd , to then broaden again and establish a hot-shoulder.
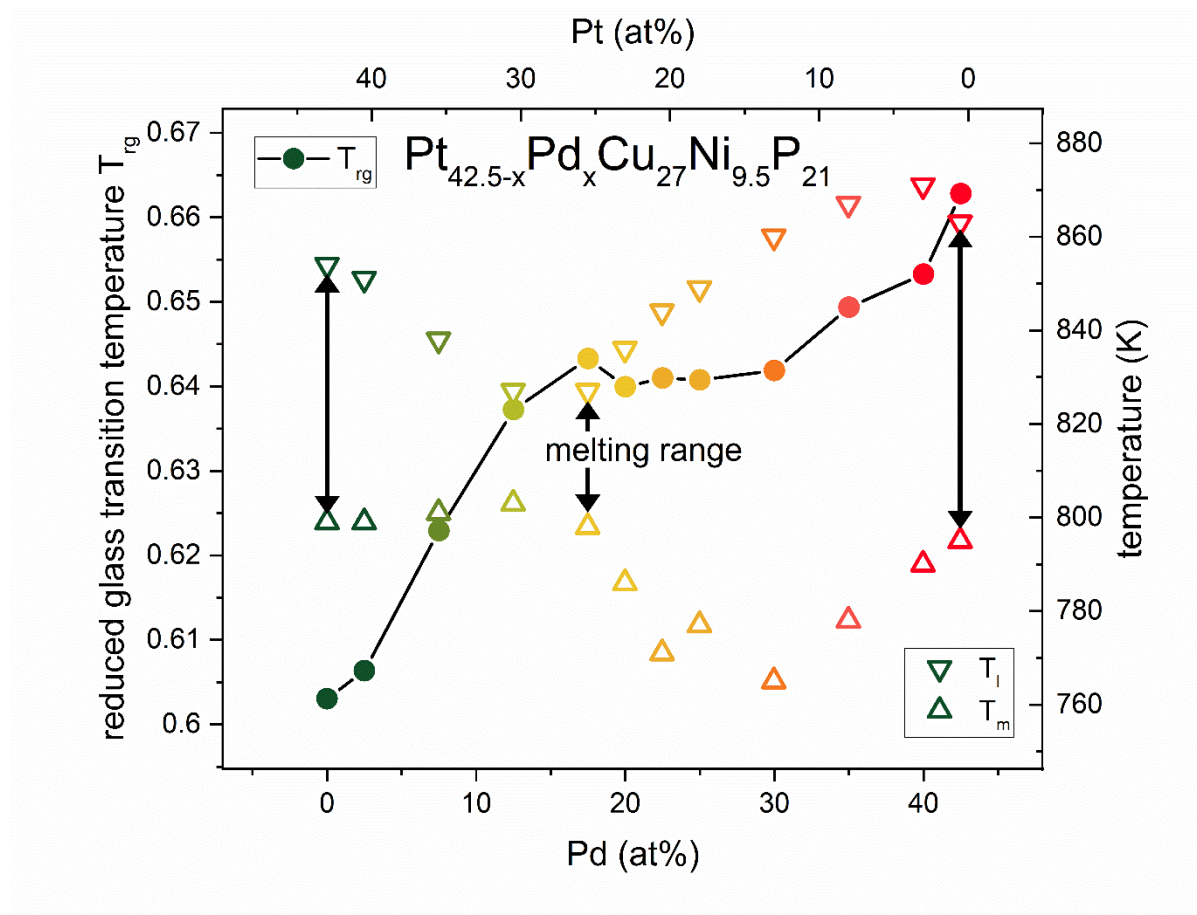
SI Figure 2: Evolution of the melting point T_m and liquidus temperature T_l (melting range) and the reduced glass-transition temperature T_{rg} as a function of Pd content. The composition showing a melting behavior closest to eutectic is found on the Pt-rich side.
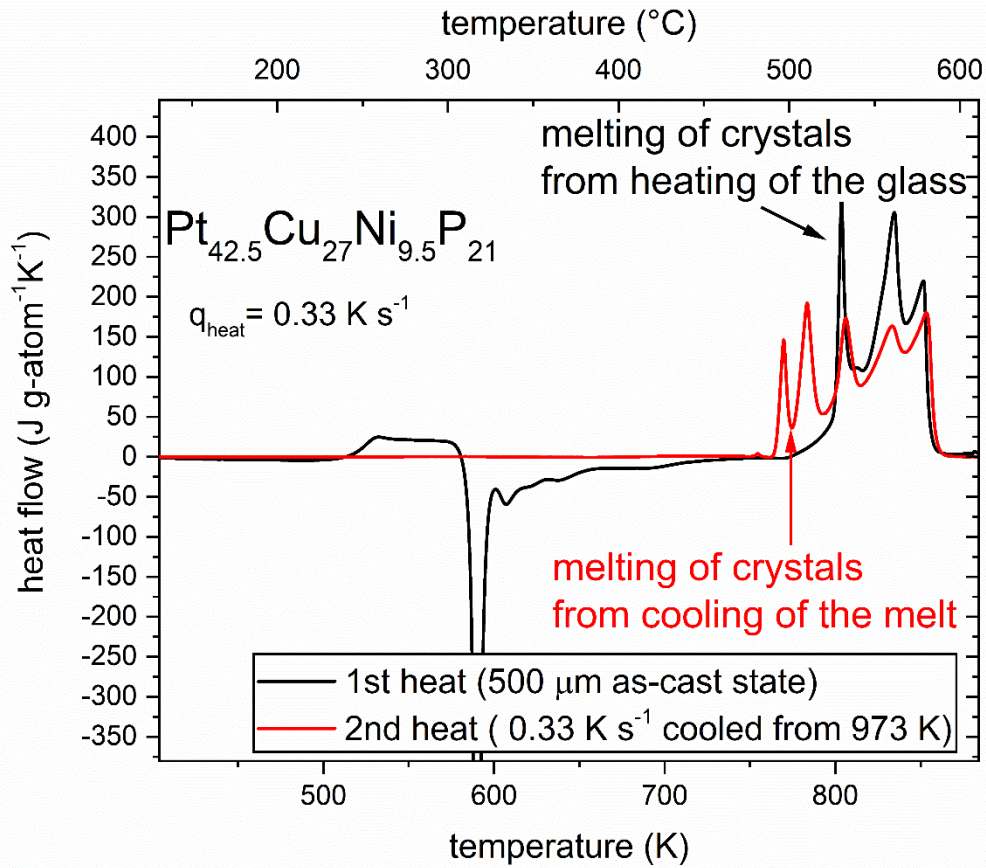
SI Figure 3: Thermograms from DSC measurements of $Pt_{42.5}Cu_{27}Ni_{9.5}P_{21}$. The different calorimetric melting signal for the melting of the crystalline phases originating from the initial glassy state (as-cast) in heating compared to the melting of crystals originating from crystallization through slow cooling (0.33 K s^{-1} < R$_{critical}$) from the equilibrium liquid state is shown.

912
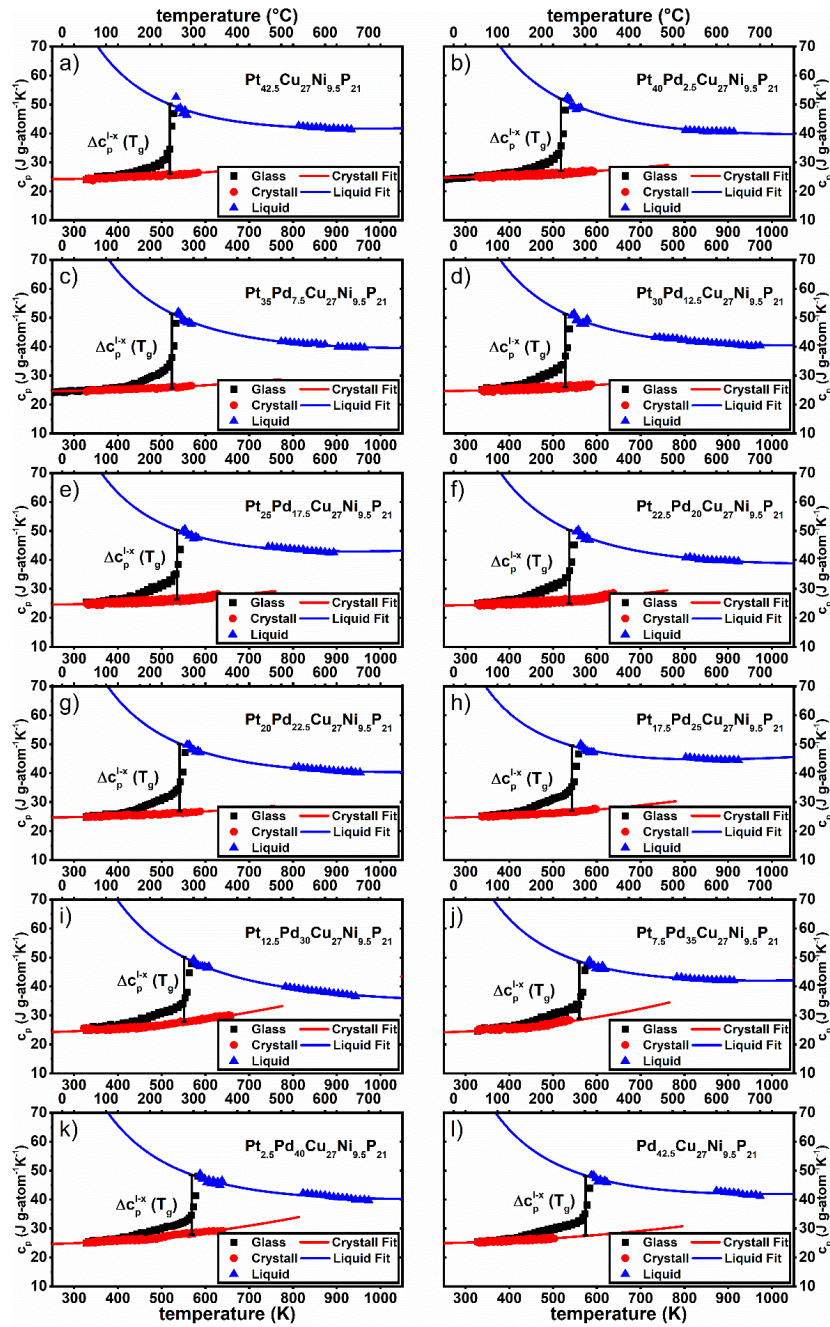
SI Figure 4 Specific heat capacity of glassy c_p (open rectangle), liquid (open triangle) and crystalline state (open circle) of all twelve examined PtPdCuNiP alloys. The fits of crystalline states (full line) and liquid states (dashed line) are based on the Kubaschewski equations, compare Eq. 1 and 2. Additionally, the difference in the specific isobaric heat capacity between the liquid and crystalline state at the glass transition temperature Δc_p^{l-x} (T_g) at a heating rate of 0.33 K/s is highlighted with a black bar for each alloy.
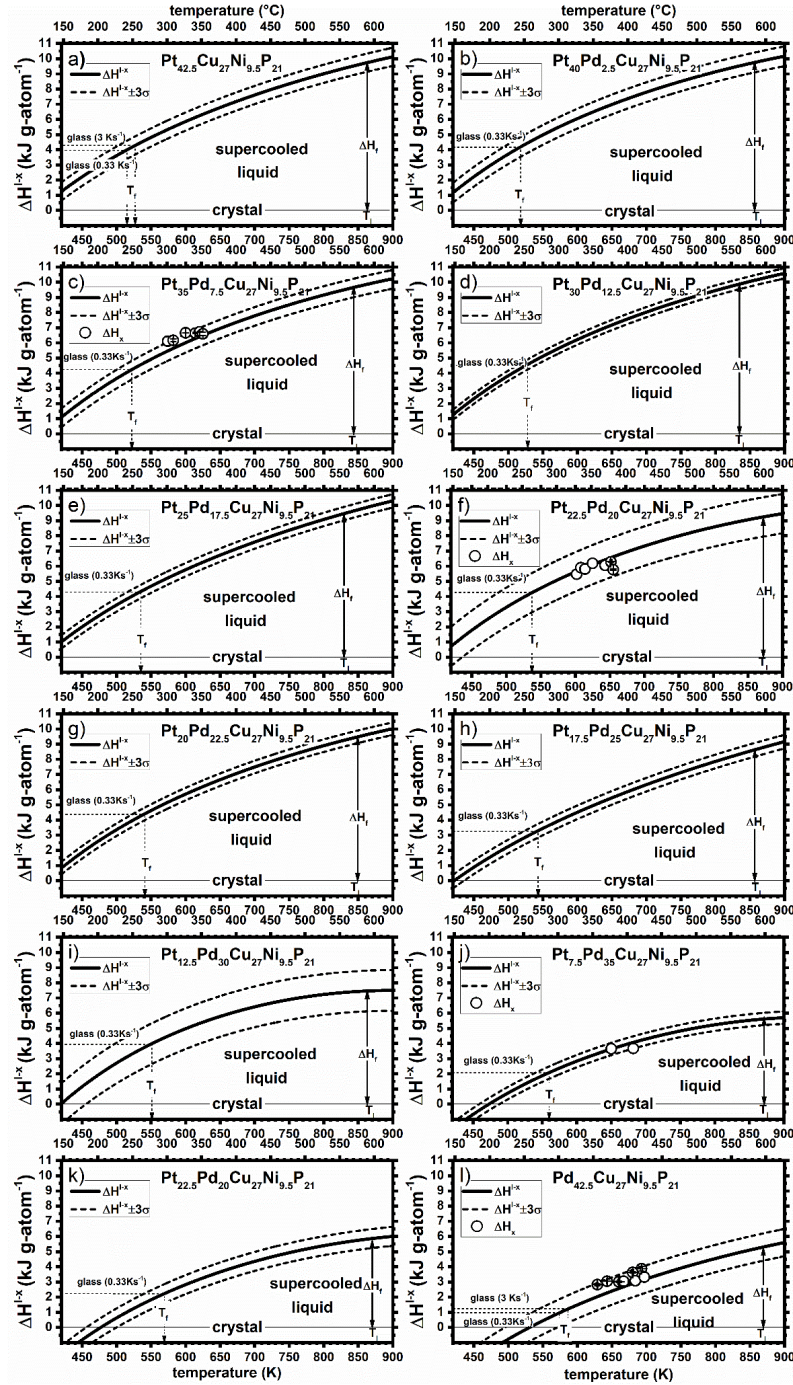
SI Figure 5: Difference in excess enthalpy between liquid and crystalline state $\Delta H^{l-x}(T)$ for all twelve examined PtPdCuNiP alloys. A confidence interval of $\pm 3\sigma$ (dashed line) is depicted to account for experimental uncertainty and crystallization enthalpies (open circles) from independent DSC measurements are inserted to support the validity of the calculation of the enthalpic curves based on the measurements of the specific isobaric heat capacity and enthalpies of melting. Further the residual enthalpies, based on the

926   **respective fictive temperature are shown for each alloy by horizontal dashed lines. It**

927   **estimates the amount of enthalpy that is stored in a glass that was has left the metastable**

928   **liquid at the given cooling rate.**

929
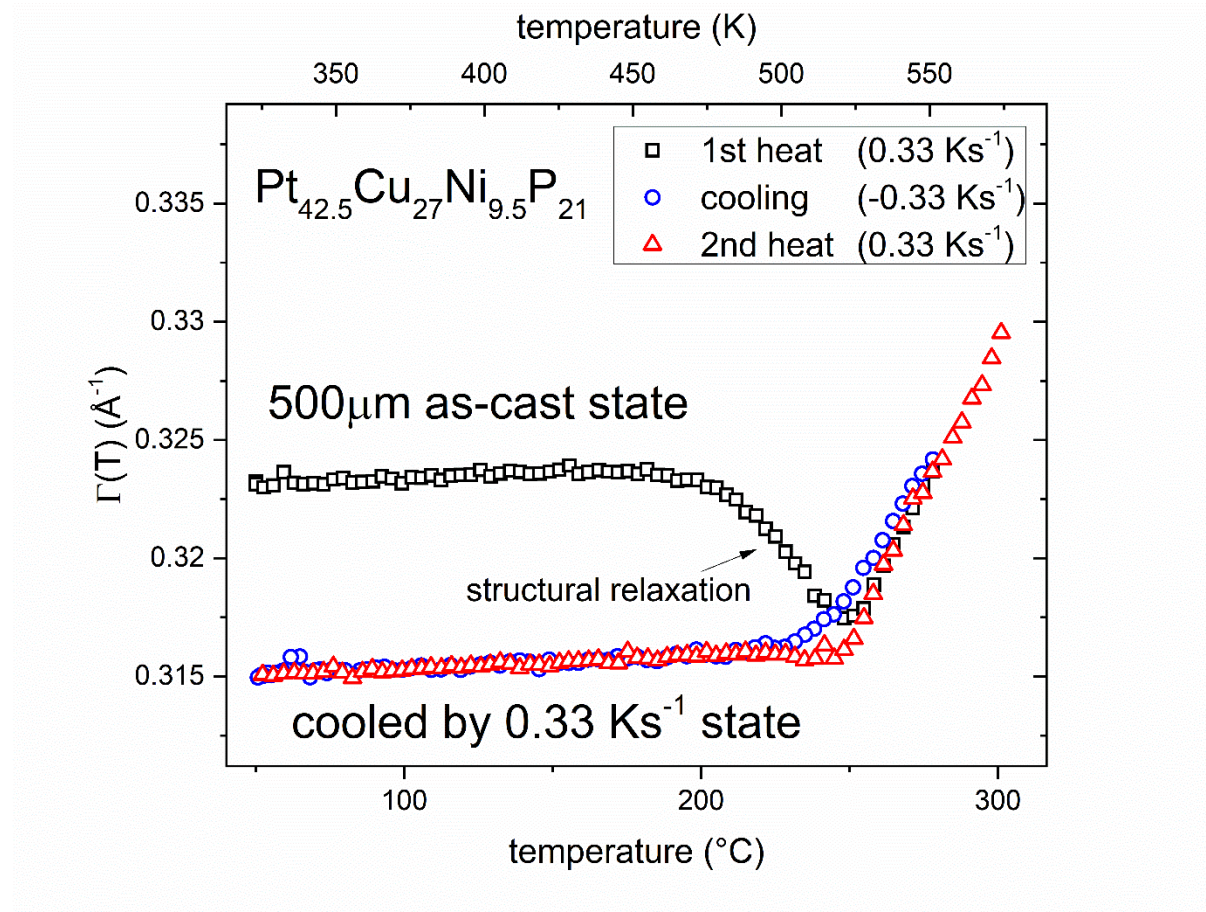
930   **SI Figure 6: Evolution of the full-width at half maximum (FWHM) of the first sharp**

931   **diffraction peak (FSDP) of the total structure factor S(Q) for the $Pt_{42.5}Cu_{27}Ni_{9.5}P_{21}$ system**

932   **during the thermal protocol of heating cooling and reheating at 0.33 K s^{-1} obtained by**

933   **high-energy X-ray diffraction. Whereas during the initial heating (1st heat, black squares)**

934   **structural relaxation close to the glass transition is apparent, this effect is not visible**

935   **during the cooling procedure (blue circles) or the reheating (2nd heat, red triangles). A**

936   **good agreement in the metastable equilibrium liquid at above ~250 °C (T_g(0.33 K s^{-}**

937   **^{1}≈244 °C) is seen in all steps.**